Study on drag and lift force acting on single bubbles rising in linear shear flows

陳, 俊名

(Degree)
博士（工学）

(Date of Degree)
2023-03-25

(Date of Publication)
2024-03-01

(Resource Type)
doctoral thesis

(Report Number)
甲第8642号

(URL)
https://hdl.handle.net/20.500.14094/0100482390

Doctoral Dissertation

Study on drag and lift force acting on single bubbles rising in linear shear flows

せん断流中単一気泡の揚力係数及び抗力係数に関する研究

January 2023

Graduate School of Engineering,
Kobe University

Chen Junming
陳俊名

Contents

Chapter 1 Introduction 1
1.1 Background ···· 1
1.2 Drag force acting on single bubbles rising in linear shear flows ···· 3
1.3 Lift force experienced by single bubbles rising in linear shear flows ···· 6
1.4 Purpose of this study ···· 12
1.5 Constitution of this study ···· 13
Reference ···· 14

Chapter 2 Drag force experienced by single bubbles rising in linear shear flows 16
2.1 Introduction ···· 16
2.2 Experimental database ···· 14
2.3 Discussion ···· 19
2.3.1 Effects of Surfactant on C_D ···· 19
2.3.2 Applicability of Available Drag Correlations ···· 20
2.3.3 Drag Correlation for Contaminated Bubbles ···· 23
2.3.4 Drag correlation for clean bubbles ···· 28
2.4 Numerical simulation of bubbles in clean systems ···· 32
2.4.1 Previous data ···· 32
2.4.2 Governing equations ···· 34
2.4.3 Numerical method and conditions ···· 35
2.4.3 Comparison between predictions and experimental data ···· 36
2.5 Summary ···· 38
Reference ···· 39

Chapter 3 Application of deep learning to lift coefficient of clean bubbles 41
3.1 Introduction ···· 41
3.2 Input and output layers ···· 41
3.3 K-Folds cross validation ···· 42
3.4 Training Phase ···· 46
3.5 Data extension using avaiable model ···· 50
3.6 Test phase ···· 54
3.7 Summary ···· 56
Reference ···· 57
Chapter 4 Effects of surfactant on lift coefficient of ellipsoidal bubbles in the viscous force dominant regime 59
4.1 Introduction ···· 59
4.2 Experimental method ···· 59
4.3 Results and discussion ···· 63
4.3.1 Bubble shape ···· 63
4.3.2 Bubble aspect ratio and relative velocity ···· 65
4.3.3 Lift coefficient ···· 68
4.3.4 Lift correlating ···· 72
4.4 The Application of deep learning method of contaminated data ···· 75
4.5 Summary ···· 77
Reference ···· 78

Chapter 5 Conclusions 80

Figure list

1.1 Surfactant adsorption on bubble interface 2
1.2 Void fraction distributions in bubbly pipe flows 6
1.3 Fully connected artificial neural network 10
1.4 Signal flow 11

2.1 Terminal velocities of contaminated bubbles 19
2.2 Drag coefficients of bubbles fully-contaminated with Triton X-100, 1-octanol, 1-decanol and SDS 21
2.3 Comparison between available C_D correlations and V_T data 22
2.4 Aspect ratios, E, of fully-contaminated bubbles 22
2.5 Factor $\psi = C_D/C_D^S-1$ representing inertia and shape deformation effects on C_D 25
2.6 Dependence of $C_D/C_D^S - 1$ on E 26
2.7 Correlating inertia and deformation effect factors using Re and E 27
2.8 Bubble velocities calculated using proposed C_D correlation, Eq. (2.9) 29
2.9 Inertia and deformation effect factor, ψ(Re, E), for clean bubbles 30
2.10 Comparison between calculated terminal velocities and data [1] 31
2.11 Comparison between Eq. (2.14) and (1.12) and V_T data for a wider range of M 31
2.12 Comparisons of V_T data between Liu's experiment and Aoyama's experiment 33
2.13 Comparisons between Liu's V_T data and Rastello correlation, Eq. (2.7) 33
2.14 Computational domain 36
2.15 Comparison between predictions of V_T (labeled as Sim) and experimental data 37

3.1 Loss history in K-folds cross validation in each Case (Nl, Nn). Solid line: loss in training; dashed line: loss in validation 44
3.2 Comparison of loss history between Cases (2, 10) and (3, 10). Solid line: loss in training; dashed line: loss in validation 45
3.3 Loss history in training phase for model of $N_l = 3$ and $N_n = 10$ 46
3.4 Comparison between predicted C_L with training data ($N_l = 3$ and $N_n = 10$). Closed symbols: predicted; open symbols: training data. H-pure, H-DI, and H-tap denote bubbles in pure water, deionized water, and tap water, respectively 47
3.5 Estimation errors for training data $N_l = 3$ and $N_n = 10$ 47
3.6 Lift curves drawn using trained ANN model of $N_l = 3$ and $N_n = 10$. The shape correlations of Eqs. (3.3) and (3.4) are used for E. 49
3.7 Data created using the Legendre-Magnaudet correlation, Eq. (3.6), (circles) and predictions with ANN correlation 52
3.8 Lift curves drawn using retrained ANN model. Closed symbols: predicted; open symbols: training data; cross symbols: additional data 53
3.9 Comparison between predicted C_L with test data ($N_l = 3$ and $Nn = 10$). Closed symbols: predicted; open symbols: test data 54
3.10 Estimation errors for test data $N_l = 3$ and $Nn = 10$ 55

4.1 Experimental setup 61
4.2 Bubble shapes 64
4.3 Bubble aspect ratio 66
4.4 Bubble relative velocity 66

4.5 Comparison between predicted and measured $|\boldsymbol{V}_\mathrm{R}|$ ···· 67
4.6 Lift coefficients in clean and cases of C_T = 0.10 and 0.20 mol/m^3 ···· 68
4.7 C_L in Triton X-100 case at low *Re* range ···· 69
4.8 Comparison between C_L of bubbles contaminated with Triton X-100 and those with 1-octanol ···· 70
4.9 Correlation of negative lift ···· 74
4.10 Comparison between predicted C_L with test data (N_l = 3 and Nn = 10). Closed symbols: predicted; open symbols: test data ···· 76
4.11 Estimation errors for test data N_l = 3 and Nn = 10. Dashed lines: ± 10% errors · 76

Table list

2.1 Fluid properties ······ 17
2.2 Surface tensions, σ_{eq} [mN/m], at adsorption-desorption equilibrium ······ 18

3.1 Dimensionless groups in datasets ······ 42
3.2 Numbers of hidden layers N_l and neurons N_n in each hidden layer ······ 43
3.3 Total numbers of parameters in ANN model ······ 43
3.4 Ranges of Re and Sr in training data added using Eq. (3.5) ······ 52

4.1 Fluid properties ······ 63
4.2 Mean absolute error and root mean squared error in calculated aspect ratios ······ 65
4.3 Coefficients in Eq. (4.13) ······ 74

Nomenclature

Latin symbols

C	[mol/m^3]	the concentration of surfactant
C_D	[–]	drag coefficient of a bubble
C_{DE}	[mol/m^3]	1-decanol concentration
C_L	[–]	lift coefficient of a bubble
C_O	[mol/m^3]	1-octanol concentration
C_S	[mol/m^3]	SDS concentration
C_T	[mol/m^3]	Triton X-100 concentration
C_{VM}	[–]	virtual mass force coefficient
d	[m]	sphere-volume equivalent bubble diameter
d_H	[m]	major reference length of a bubble
d_V	[m]	minor reference length of a bubble
E	[–]	the aspect ratio of a bubble
Eo	[–]	Eötvös number (reference length: d)
Eo_H	[–]	Eötvös number (reference length: d_H)
g	[m/s^2]	gravity
Ha	[–]	Hatta number
M	[–]	Morton number
P	[Pa]	pressure
Re	[–]	Reynolds number
Re_{S}	[–]	Reynolds number of solid sphere
Sr	[–]	Dimensionless shear rate
t	[s]	time
T	[^{o}C]	temperature
V	[m/s]	velocity
V_B	[m/s]	velocity of a bubble
V_L	[m/s]	velocity of liquid
$\|\boldsymbol{V}_R\|$	[m/s]	bubble velocity relative to the liquid velocity
V_T	[m/s]	terminal velocity of a bubble

Greek symbols

ϕ	[–]	shear-deformation-effect multiplier

μ	[Pa·s]	viscosity
ρ	[kg/m^3]	density
σ	[N/m]	surface tension
σ_{eq}	[N/m]	surface tension at the adsorption-desorption equilibrium
σ_0	[N/m]	surface tension of surfactant free interface
ω	[s^{-1}]	velocity gradient

Subscripts

B	bubble
G	gas
L	liquid
S	solid

Superscripts

S	Spherical bubble
H	High Reynolds numbers
L	Low Reynolds numbers

Chapter 1

Introduction

1.1 Background

Flowing liquid, unlike solid that keeps its shape, has driven the passion of researchers for centuries since the first principle of fluid dynamics was stated by Bernoulli. Rising in the continuous phase, bubbles, which gain kinetic energy due to buoyancy and the interaction between the two phases, bear great importance since that two-phase flows appears prevalently in industrial applications such as bubbly flows in a bubble column and a cooling system in a nuclear plant. Interaction between two-phases, macroscopically epitomized as shear and pressure forces, plays an important role in determining bubble motion. Therefore, to achieve the optimization of industrial systems with respect to their efficiency and safety, knowledge on those forces is of indispensable significance.

Net force acting on single bubbles can be orthogonally decomposed into drag and lift forces. A bubble rising in liquid experiences the drag force in the vertical direction. Available correlations of the drag force, although adopting complex form, are applicable to a limited range of bubble diameters and fluid properties. Recent knowledge on the effects of the viscosity, bubble shape deformation, etc. paves the way to accurate and concise correlations of the drag force coefficient (C_D) applicable to a wide range of the bubble Reynolds number in both clean and contaminated systems.

In pipe flows, shear stress between the pipe wall and the liquid results in nonuniform velocity fields. Linear shear flow is one of these fields. Rising in such flows, a bubble exhibits lateral migration which is caused by the lift force. In co-current upward bubbly flows, a positive sign of the lift coefficient causes bubble migration to the place where the liquid flow has a lower vertical velocity while a negative sign does the opposite. Due to the complexity of forces exerted by the surrounding liquid, research on the lift force remains insufficient in both analytical and experimental aspects. Not only the nonuniform velocity fields but also the impurity in liquid cause changes in C_D and C_L of single bubbles. As shown in **Fig. 1.1**, Surfactants accumulating at the interface between the gas and liquid make the interface immobile and prevent internal circulation in the bubble, which makes a bubble behave like a solid particle. Concentration gradient of surfactant along the interface results in Marangoni force. Therefore, to gain better accuracy in the prediction of bubbly flows, the effects of surfactants shall be considered. In this study two types of surfactants were used in the experiments.

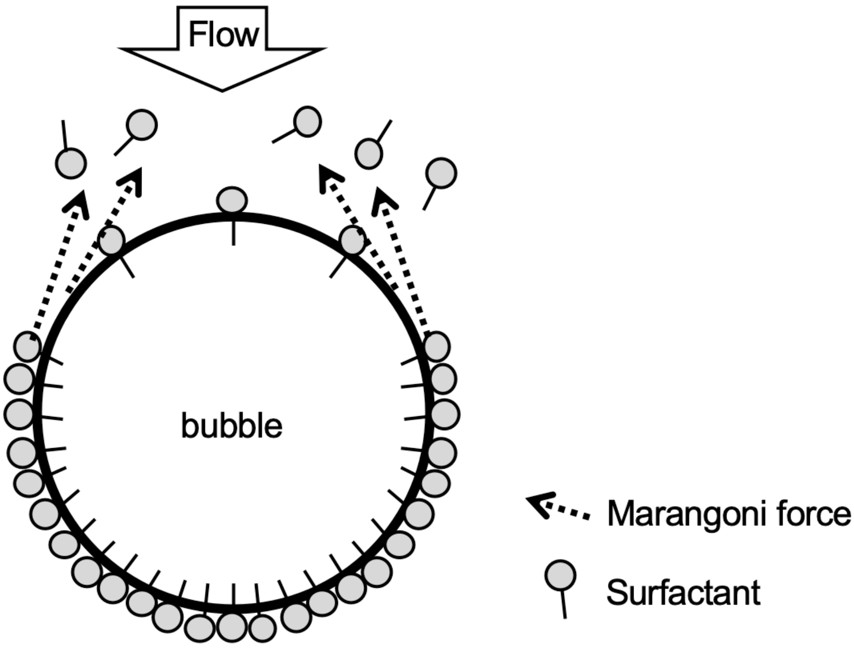

Fig 1.1: Surfactant adsorption on bubble interface

1.2 Drag force acting on single bubbles

Gas bubbles in liquids are encountered in a wide range of flows in practical realm. A reliable model of the drag force acting on a bubble in infinite stagnant liquid is a prerequisite for accurate prediction of gas-liquid two-phase bubby flows. Since surface-active agents (surfactants) are often present in industrial systems, modeling of the effects of surfactant on the drag force is of great importance.

Single bubbles rising in liquid eventually reach an equilibrium state in the vertical direction due to the balance between the buoyancy and the drag force:

$$C_D \frac{1}{2}\rho_L V_T^2 \frac{\pi d^2}{4} = (\rho_L - \rho_G) g \frac{\pi d^3}{6} \tag{1.1}$$

Eq. (1.1) is a scalar equation equating the drag force on the left-hand side and the buoyancy on the right-hand side, where the subscripts G and L denote the gas and liquid phases, respectively, C_D the drag coefficient, V_T the terminal velocity, ρ the density and d the sphere-volume equivalent bubble diameter. Re-arranging Eq. (1.1) yields:

$$C_D = \frac{4(\rho_L - \rho_G) g d}{3\rho_L V_T^2} \tag{1.2}$$

Eq. (1.2) shows that the drag coefficient can be computed by measuring the terminal velocity.

Dimensionless parameters are often used to describe bubble motion, The definitions of the relevant dimensionless groups are given below:

$$Re = \frac{\rho_L V_T d}{\mu_L} \tag{1.3}$$

$$Eo = \frac{\Delta\rho g d^2}{\sigma} \tag{1.4}$$

$$Sr = \frac{\omega d}{V_T} \tag{1.5}$$

$$E = \frac{d_{\mathrm{V}}}{d_{\mathrm{H}}} \tag{1.6}$$

where μ is the viscosity, $\Delta\rho$ the density difference between the two phases, σ the surface tension, ω the velocity gradient of liquid shear flow, d_{V} and d_{H} the horizontal and verticle reference length of a bubble, and $d=(d_{\mathrm{V}}d_{\mathrm{H}}^2)^{1/3}$

Factors such as bubbles shape, fluid properties, surface tension, liquid velocity profile and internal circulation contribute to the distribution of shear force and pressure at the interface between the gas and liquid. Moreover, pure liquid rarely exists. Surfactants are unintentionally present or sometimes intentionally added to the liquid in practical systems. The accumulation of surfactants at the interface may change bubble motion. To achieve better accuracy by considering the factors mentioned above, available correlations were proposed at the cost of increasing complexity.

Schiller-Naumann [1] suggested to use the following drag correlation for solid spheres:

$$C_{D\mathrm{S}} = \frac{24}{Re_{\mathrm{S}}}\left[1+0.15Re_{\mathrm{S}}^{0.687}\right] \tag{1.7}$$

where the subscript S denotes solid. For clean bubbles in the viscous-force dominant regime, Tomiyama et al. [2] proposed the following C_D correlation:

$$C_D = \frac{16}{Re}\left[1+0.15Re^{0.687}\right] \tag{1.8}$$

where the factor, $1+0.15Re^{0.687}$, is a modification to the Stokes drag. Here, shape deformation of a bubble is not considered. Shape deformation of a bubble is characterized by aspect ratio E ($=d_{\mathrm{V}}/d_{\mathrm{H}}$), where d_{V} and d_{H} are the minor and major reference length of a bubble. Milizer et al. [3] proposed the following $C_{D\mathrm{S}}$ correlation for ellipsoidal particles for $1 < Re_{\mathrm{S}} < 200$:

$$C_{DS}=\frac{24}{Re_S}\left[\left(1+0.15Re_S^{0.687}\right)+\frac{2}{1+42500Re_S^{-1.16}}\right]\phi(Re_S,E) \tag{1.9}$$

where ϕ is the shape-deformation-effect multiplier given by

$$\phi(Re_S,E)=1+0.00096\frac{Re_S}{E}-0.000754Re_S E+\frac{0.0924}{Re_S}+0.0027E^2 \tag{1.10}$$

Other correlations [4],[5] taking shape deformation into account adopt the forms as shown below:

$$C_D=\frac{48G(E)}{Re}\left[1+\frac{H(E)}{\sqrt{Re}}\right] \tag{1.11}$$

$$C_D=\frac{16}{Re}\left[\frac{1+\frac{8(1-E)}{15E}+0.015(3G(E)-2)Re}{1+0.015Re}+\left[\frac{8}{Re}+\frac{1}{2}\left(1+\frac{3.315H(E)G(E)}{Re^{0.5}}\right)\right]^{-1}\right] \tag{1.12}$$

where $G(E)$ and $H(E)$ are functions of E and Loth [6] proposed the following approximations for them:

$$G(E)=0.1287+0.4256/E+0.4466/E^2 \tag{1.13}$$

$$H(E)=0.8886+0.5693/E-0.4563/E^2 \tag{1.14}$$

Correlations above are complicated and limited to a narrow range of Re. Therefore, in chapter 2, a simpler but accurate correlation applicable to a wide range of Re is developed.

1.3 Lift force experienced by single bubbles rising in linear shear flows

A bubble experiences the lift force when moving in shear flow. Bubbles migrating in the lateral direction while rising in a pipe flow form non-uniform void distributions as shown in **Fig. 1.2**. Small bubbles tend to migrate to the wall while large ones tend to gather in the center.

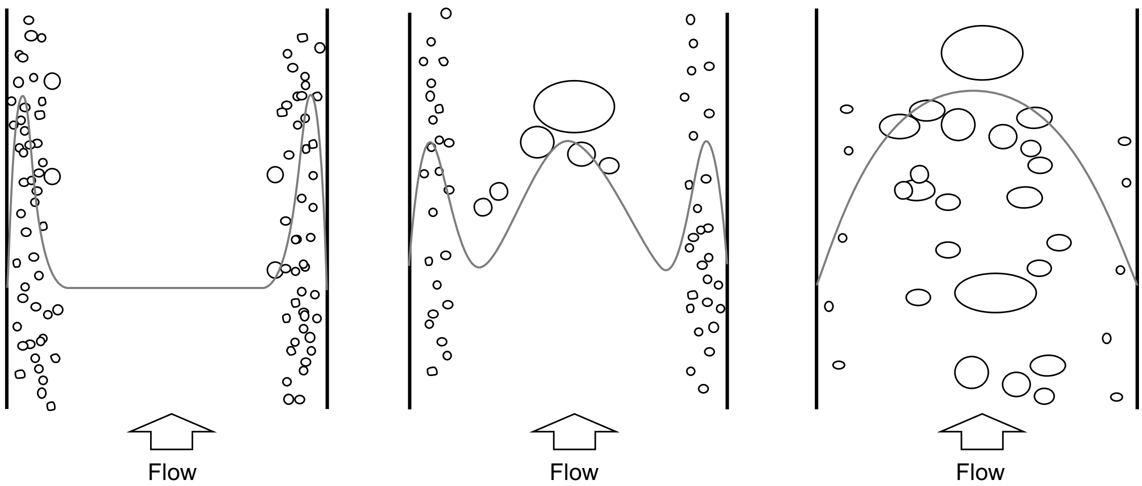

(a) Wall-peak (b) Double-peak (c) Core-peak

Fig 1.2 Void fraction distributions in bubbly pipe flows

The equation of bubble motion is given by:

$$\left(\rho_G+C_{VM}\rho_L\right)\frac{\mathrm{d}\boldsymbol{V_B}}{\mathrm{d}t}=-\frac{3C_D\rho_\mathrm{L}|\boldsymbol{V_R}|\boldsymbol{V_R}}{4d}-C_L\,\rho_\mathrm{L}\,\boldsymbol{V_R}\times\mathrm{curl}\boldsymbol{V_L}+\left(\rho_L-\rho_G\right)\boldsymbol{g} \tag{1.15}$$

where, ρ is the density, C_{VM} the virtual mass force coefficient, $\boldsymbol{V_B}$ the bubble velocity, $\boldsymbol{V_L}$ the liquid velocity, $\boldsymbol{V_R}$ the relative velocity between bubble and liquid, t the time, $\boldsymbol{g}$ the gravity. The subscript B, G and L denote the bubble, the gas and the liquid respectively. Experimental data of $\boldsymbol{V_B}$, $\boldsymbol{V_L}$, $\boldsymbol{V_R}$ and d were used to compute the lift coefficient (C_L) via Eq. (1.15). Moreover, implicit relationship between the drag and lift force of a bubble is hidden in Eq. (1.15) and will be discussed in Sec. 4.

Available correlations of the lift coefficient are listed below:

$$C_L^S = 0.5 \tag{1.16}$$

$$C_L^{SH} = \frac{1}{2}\left(\frac{1+\frac{16}{Re}}{1+\frac{29}{Re}}\right) \tag{1.17}$$

$$C_L^{SL} = \frac{6}{\pi^2}\frac{2.255}{\sqrt{SrRe}\left(1+\frac{0.2Re}{Sr}\right)^{1.5}} \tag{1.18}$$

$$C_L^S = \left(\left[C_L^{SL}\right]^2 + \left[C_L^{SH}\right]^2\right)^{0.5} \tag{1.19}$$

where the superscripts *S*, *H*, *L* denote a spherical bubble, high Reynolds numbers and low Reynolds numbers respectively. Eq. (1.16) is derived analytically by Auton [7]. Eqs. (1.17), (1.18) and (1.19) are suggested by Legendre and Magnaudet [8] via numerical simulation. Eq. (1.17) applies to a low *Re* bubble while Eq. (1.18) applies to a high *Re* bubble. Eq. (1.19) is the combination of Eqs. (1.17) and (1.18).

Shape deformation of a bubble is one of the important factors that affects the C_L. Naciri [9] showed that the C_L of a bubble of non-deformable ellipsoidal shape in a weak inviscid shear flow increases with increasing the shaped deformation. Based on that, Adoua et al. [10] suggested an empirical correlation:

$$C_L = \frac{1}{2} g_N(E) \tag{1.20}$$

where g_N is the deformation effect multiplier given by

$$g_N = 1 + 1.22\left(\frac{1}{E} - 1\right) \tag{1.21}$$

This correlation can be regarded as an extension of Auton's solution for a spherical bubble at high *Re*. Tomiyama et al. [11] considered the deformation effect by using the major axis, d_H, of a bubble as the reference length scale to correlate C_L:

$$C_L = \begin{cases} \min\left[0.288\tanh(0.121Re)\,, f_{\mathrm{T}}(Eo_H)\right] & \text{for} \quad Eo_H < 4 \\ f_{\mathrm{T}}(Eo_H) & \text{for} \;\; 4 < Eo_H < 10.7 \end{cases} \tag{1.22}$$

where

$$f_T(Eo_H)\text{=}0.00105Eo_H{}^3\text{-}0.0159Eo_H{}^2\text{-}0.0204Eo_H\text{+}0.474 \tag{1.23}$$

and Eo_H is the Eötvös number defined by

$$Eo_H\text{=}\frac{\Delta\rho g d_H{}^2}{\sigma} \tag{1.24}$$

Dijkhuizen et al. [12] carried out numerical simulations of single bubbles in linear shear flows and correlated C_L in the following form:

$$C_L\text{=}\min\left[C_L^S, f_D(Eo_H)\right] \tag{1.25}$$

$$f_{\mathrm{D}}(Eo_H)\text{=}0.5 - 0.11Eo_H\text{+}0.002Eo_H{}^2 \tag{1.26}$$

where C_L^S is given by Eq. (1.17).

Ziegenhein et al. [13] and Lucas and Ziegenhein [14] proposed the following empirical correlation for $Eo_{\mathrm{H}} > 1.2$:

$$C_L\text{=}\max\left[f_Z(Eo_H),\; -0.33\right] \tag{1.27}$$

$$f_Z(Eo_{\mathrm{H}})\text{=}0.5 - 0.1\, Eo_H + 0.002\, Eo_H{}^2 \tag{1.28}$$

where the second coefficient of f_Z was slightly modified from that of f_D by fitting the functional form to Ziegenhein's data for bubbles in a low viscosity system. The above lift correlations are mainly focus on singe bubbles in a clean system and are rarely supported by experimental data. To predict practical bubbly flows, correlations for a contaminated systems is of practical importance.

It is well-known that surfactant affects bubble shapes and bubble motion [15],[16]. The surfactant decreases the surface tension and the gradient of surface tension causes a tangential force to the interface, i.e. the Marangoni force, which weakens interfacial velocity and shape deformation of the bubble. The presence of surfactant also affects C_L of bubbles in linear shear flows. Hayashi and Tomiyama [17] considered surfactant effects on C_L of spherical and ellipsoidal bubbles for the ranges of $2 < Re < 70$ and $Sr < 1$ using the level set method. A sign reversal of C_L occurs at lower Re and Eo, compared with clean bubbles. They also pointed out that the Hatta number, Ha, which is the ratio of the adsorption rate to the bubble rise velocity, is an important factor to consider C_L of contaminated bubbles: C_L of high Ha bubbles can be correlated in terms of a modified Eötvös number using the surface tension reduced by surfactant, whereas the Marangoni force has to be taken into account for C_L of low Ha bubbles. Hayashi et al. [18],[19] proposed lift correlations applicable to bubbles in clean systems. However, no correlation is available for contaminated systems.

To understand the lift force acting on a bubble in contaminated systems, experimental data are indispensable. Hence experiments on single contaminated bubbles in linear shear flows are carried out in this study. To consider a limiting case opposite to clean bubbles, bubbles are fully contaminated. The drag coefficients of a bubble agree with those of solid particles. The applicability of available correlations of the drag coefficient, C_D, and the aspect ratio, E, to the present systems are examined, and the correlation of C_L in contaminated systems will be proposed.

With adequate data, artificial neural network (ANN) can be applied to generate additional data via an optimized training model. The key for realizing a reliable and widely applicable ANN correlation is to accumulate a large number of data. In addition, deep learning has been utilized in a wide variety of scientific fields. In the multiphase flow community, deep learning techniques, especially the artificial neural network [20], have been utilized. As for the bubble dynamics, an ANN correlation is expected to give good evaluations of model coefficients in the constitutive equations such as the drag, lift, and so on, which are required in bubbly flow simulations based on the averaging models. This study also aims to clarify the capability of an ANN correlation to express the lift coefficients of spherical and deformed bubbles in linear shear flows.

The ANN used in this study consists of the input layer with N inputs, $\boldsymbol{x}$ (= (x_1, x_2, · · · , x_N)), the Affine layers having the weight matrix $\boldsymbol{W}$ and the bias $\boldsymbol{b}$, the batch-normalization layer [21], the leaky ReLU (leaky rectified linear unit) layer [22], and the identity layer for the output (**Figs. 1.3** and **1.4**). All the layers are fully connected. The $\boldsymbol{x}$ is weighted and biased by using $\boldsymbol{W}$ and $\boldsymbol{b}$ to transform it into the signal $\boldsymbol{a}$ and then is transferred to the neurons in the first hidden layer:

$$a_i = x_j W_{ji} + b_i \tag{1.29}$$

where W_{ji} are the component of the weight matrix connecting the jth input and the ith neuron in the hidden layer, and b_i is the ith component of $\boldsymbol{b}$. Batch-Norm is applied to the signal $\boldsymbol{a}$ as

$$\bar{a}_i = \frac{a_i - \mu_{Bi}}{\sigma_{Bi}} \tag{1.30}$$

where μ_B and σ_B are the mean and the standard deviation of a in the batch. The $\hat{a}$ is scaled by the trainable coefficients $\boldsymbol{\gamma}$ and $\boldsymbol{\beta}$ as

$$\hat{a}_i = \gamma_i \bar{a}_i + \beta_i \tag{1.31}$$

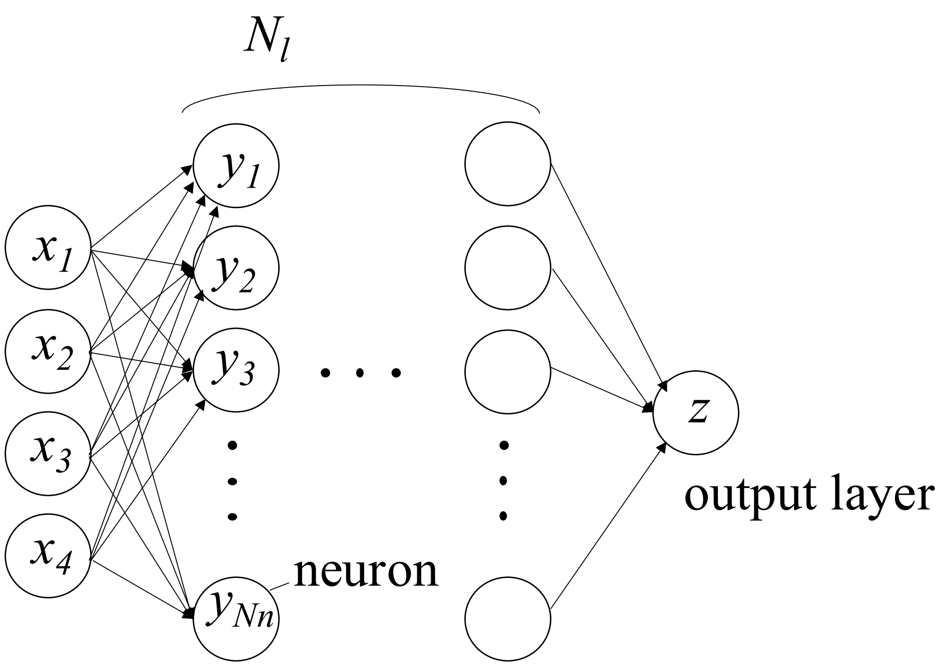

Fig. 1.3 Fully connected artificial neural network

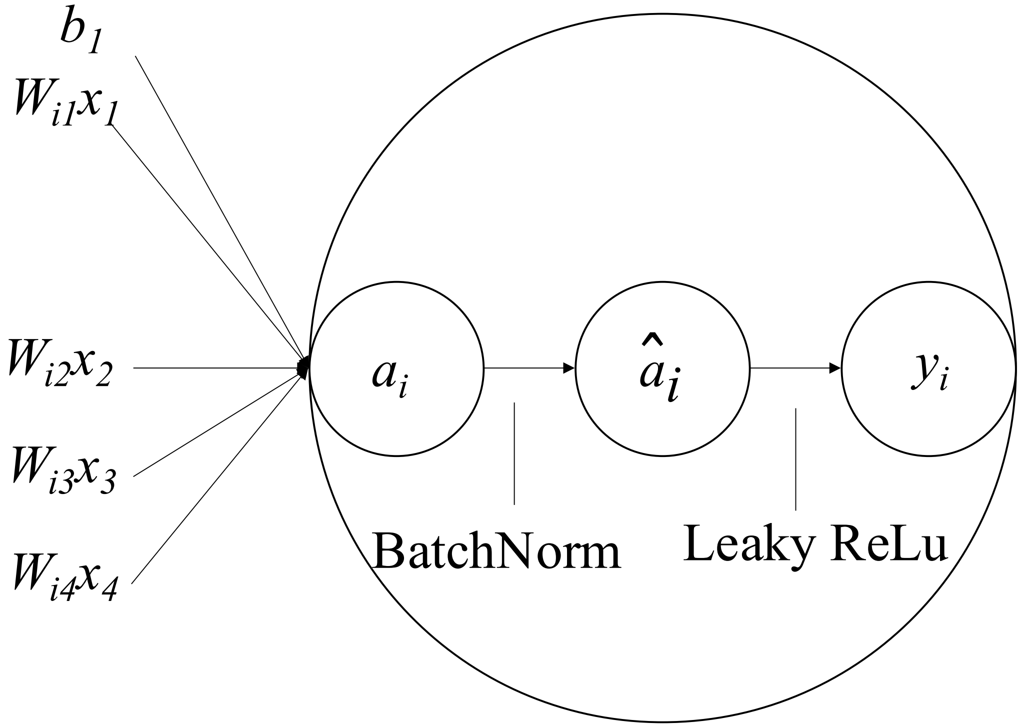

Fig. 1.4 Signal flow

The leaky ReLU is then applied to $\hat{a}$:

$$y_i = \begin{cases} \hat{a}_i & \text{for } \hat{a} \geq 0 \\ \alpha\hat{a}_i & \text{for } \hat{a} < 0 \end{cases} \tag{1.32}$$

where the gradient for the negative signals is given by $\alpha = 0.01$. The signal y goes to the next hidden layer. The output layer applies the identity function, and the output is denoted by z.

The ANN is trained by using the gradient descent learning. The NAG (Nesterov accelerated gradient) algorithm [23] is used for learning. The weight parameters are initialized using Gaussian distribution [24]. The mean squared error is used as the loss function for evaluating the performance of the ANN.

1.4 Purpose

Bubble dynamics is strongly affected by impurities and shear fields in the system. Effects of surfactants and shear fields on the drag and lift force of a bubble is therefore of great importance. Available correlations of the drag force are complicated and limited to a narrow applicable range. The knowledge on the lateral motions of single bubbles in contaminated system is still insufficient due to few relevant experimental data. To realize accurate simulations of bubbly flows, concise and reliable correlations of C_D and C_L are indispensable.

The purpose of this study is to develop simple and reliable correlations of the drag and lift forces of a bubble based on experimental data. To achieve this purpose, experiments are conducted with the presence of several kinds of surfactants. Experimental data in contaminated systems are obtained. Numerical and artificial intelligence methods are also employed.

1.5 Constitution of the dissertation

There are five chapters in this dissertation. Below is the brief introduction of each chapter.

Chapter 1 introduces available knowledge on the drag and lift forces of a bubble. In this chapter, the importance of reliable and concise correlations of the drag and lift forces of a bubble is illustrated. The limitation of the available correlations is discussed. The methods and purpose of this study are summarized.

Chapter 2 deals with the drag correlation for single bubbles rising in linear shear flow. Available correlations of the drag coefficient are complicated and limited to a relatively low range of Reynold numbers. Under both clean and contaminated systems, reliable and simple drag correlations applicable to a wide range of Reynold numbers are suggested.

Chapter 3 demonstrates the application of deep learning method to experimental data of lift coefficients. An artificial neural network (ANN) method for generating the lift coefficients of spherical and deformed bubbles in linear shear flows is developed, which clarifies the capability of an ANN correlation to express the lift coefficients of spherical and deformed bubbles in linear shear flows.

Chapter 4 focuses on the lift force of a bubble in contaminated systems. Due to the lack of experimental data, the lift coefficient of a bubble in contaminated systems was remained uncertain. The experiments in this chapter extends the lift database for a bubble rising in contaminated systems. Factors such as the fluid properties, surfactants and shear rates, etc. are considered to generate an accurate lift correlation applicable to a wide range of Reynold numbers.

Chapter 5 is the conclusions of this dissertation.

Reference

[1] Schiller, L., Naumann, A.Z., 1933. Über die grundlegenden Berechnungen bei der Schwerkraftaufbereitung, Zeitschridt des Vereines Deutscher Ingenieure, 44, 318-320.

[2] [2] Tomiyama, A., Kataoka, I., Zun, I., Sakaguchi, T., 1998. Drag Coefficients of Single Bubbles under Normal and Micro Gravity Conditions, JSME International, 41(2), 472-479.

[3] Militzer, J., Kan, J. M., Hamdullahpur, F., Amyotte, P. R., Al Taweel, A. M., 1989. Drag Coefficient for Axisymmetric Flow around Individual Spheroidal Particles, Powder technology, 57, 193-195.

[4] Moore, D. W. 1965. The Velocity Rise of Distorted Gas Bubbles in a Liquid of Small Viscosity, Journal of Fluid Mechanics, 23, 749-766.

[5] Rastello, M., Marié, J.-L., Lance, M., 2011. Drag and Lift Forces on Clean Spherical and Ellipsoidal Bubbles in a Solid-Body Rotating Flow, Journal of Fluid Mechanics, 682, 434-459.

[6] Loth, E., 2008, Drag of Non-Spherical Solid Particles of Regular and Irregular Shape, Powder Technology, 182(3), 342-353.

[7] Auton, T. R., Hunt, J. C. R., Prud'homme, M., 1988. The force exerted on a body in inviscid unsteady non-uniform rotational flow. Journal of Fluid Mechanics 197, 241–257.

[8] Legendre, D., Magnaudet, J., 1998. The lift force on a spherical bubble in a viscous linear shear flow. Journal of Fluid Mechanics 368, 81–126.

[9] Naciri, A., 1992. Contribution \`a l'´etude des forces exerc´ees par un liquide sur une bulle de gaz: portance, masse ajout´ee et interactions hydrodynamiques. Ph.D. thesis, Ec. Centrale Lyon, France.

[10] Adoua, R., Legendre, D., Magnaudet, J., 2009. Reversal of the lift force on an oblate bubble in a weakly viscous linear shear flow. Journal of Fluid Mechanics 628, 23–41.

[11] Tomiyama, A., Tamai, H., Zˇun, I., Hosokawa, S., 2002. Transverse migration of single bubbles in simple shear flows. Chemical Engineering Science 57, 1849–1858.

[12] Dijkhuizen, W., van Sint Annaland, M., Kuipers, J. A. M., 2010. Numerical and experimental investigation of lift force on single bubbles. Chemical Engineering Science 65, 1274–1287.

[13] Ziegenhein, T., Tomiyama, A., Lucas, D., 2018. A new measuring concept to determine the lift force for dis- torted bubbles in low Morton number system: Results for air/water.

International Journal of Multiphase Flow 108, 11–24.

[14] Lucas, D., Ziegenhein, T., 2019. Influence of the bubble size distribution on the bubble column flow regime.International Journal of Multiphase Flow 120, 103092.

[15] Tomiyama, A., Tamai, H., Zˇun, I., Hosokawa, S., 2002. Transverse migration of single bubbles in simple shear flows. Chemical Engineering Science 57, 1849–1858.

[16] Aoyama, S., Hayashi, K., Hosokawa, S., Lucas, D., Tomiyama, A., 2017. Lift force acting on single bubbles in linear shear flows. International Journal of Multiphase Flow 96, 113–122.

[17] Hayashi, K., Tomiyama, A., 2018. Effects of surfactant on lift coefficients of bubbles in linear shear flows. International Journal of Multiphase Flow 99, 86–93.

[18] Hayashi, K., Hessenkemper, H., Lucas, D., Legendre, D., and Tomiyama, A., Scaling of Lift Reversal of Deformed Bubbles in Air-Water Systems, Int. J. Multiphase Flow, vol. 142, p. 103653, 2021.

[19] Hayashi, K., Legendre, D., and Tomiyama, A., Lift Coefficients of Clean Ellipsoidal Bubbles in Linear Shear Flows, Int. J. Multiphase Flow, vol. 129, p. 103350, 2020.

[20] Beale, R. and Jackson, T., Neural Computing: An Introduction, New York: IOP Publishing, 1990.

[21] Ioffe, S. and Szegedy, C., Batch Normalization: Accelerating Deep Network Training by Reducing Internal Covariate Shift, Proc. of the 32nd Int. Conf. on Machine Learning, F. Bach and D. Blei (Eds.), Vol. 37 of Proceedings of Machine Learning Research, PMLR, Lille, France, pp. 448–456, 2015.

[22] Maas, A.L., Hannun, A.Y., and Ng, A.Y., Rectifier Nonlinearities Improve Neural Network Acoustic Mod- els, Proc. of the 30th Int. Conf. on Machine Learning, Atlanta, Georgia, USA, 2013.

[23] Nesterov, Y., A Method for Unconstrained Convex Minimization Problem with the Rate of Convergence O(1/k2), Dokl. Akad. Nauk SSSR, vol. 269, no. 3, pp. 543–547, 1983.

[24] He, K., Zhang, X., Ren, S., and Sun, J., Delving Deep into Rectifiers: Surpassing Human-Level Perfor- mance on ImageNet Classification, Proc. of 2015 IEEE Int. Conf. on Computer Vision (ICCV), Santiago, Chile, 2015.

Chapter 2

Drag force experienced by single bubbles

2.1 Introduction

Individual sample of rising bubble contains multiple features, which results in complicated correlations of C_D. Moreover, pure liquid rarely exists. Surfactants are added to the continuous phase for gaining a better practical knowledge on bubble dynamics since that accumulating at the interface of gas and liquid renders bubbles to behave like a solid sphere. In practice, complicated correlations can be easily obtained due to the large variety of features. As illustrated in Chapter 1, many correlations of C_D were suggested. However, they are both complicated and limited in application.

In this Chapter, the effects of the shape deformation on C_D of fully-contaminated ellipsoidal bubbles rectilinearly rising through infinite stagnant liquids is investigated to develop a simple but accurate C_D correlation applicable to a wide range of Reynold numbers for practical applications.

2.2 Experimental database

Experimental data of terminal velocities of single ellipsoidal bubbles contaminated with surfactant [1] are used for developing a C_D correlation. The outline of the experiment and the experimental conditions are described in this section. The test section was a water container, whose size was 0.20, 0.20 and 0.69 m in width, depth and height, respectively. The container size was large enough to make the wall effect on the bubble motion negligible. Air was used for the gas phase. Single bubbles were formed at the bottom of the container by injecting air from a syringe through a nozzle. Several nozzles with diameters ranging from 0.51 to 4.0 mm were used to form bubbles of various diameters. Water purified by a Millipore system (Elix3) and pure glycerol were mixed and used for the liquid phase. The experiments were carried out at room temperature (25°C) and atmospheric pressure. **Table 2.1** shows the fluid properties of the liquid phase, where M is the Morton number defined by

$$M=\frac{\mu_L^4(\rho_L-\rho_G)g}{\rho_L^2\sigma^3} \tag{2.1}$$

where ρ is the density, μ the viscosity, g the acceleration of gravity, σ the surface tension, σ_0 the surface tension of surfactant free interface, and the subscripts L and G denote the liquid and gas phases, respectively.

Table 2.1 Fluid properties

$\log M(\sigma_0)$	ρ_L [kg/m^3]	μ_L [mPa·s]	σ_0 [mN/m]
−8.0	1116	4.4	69
−6.7	1154	9.3	68
−3.9	1205	46.7	67

*The ρ_G and μ_G are 1.2 kg/m^3 and 1.8x10^{-5} Pa·s at 25 °C.

A high-speed video camera (Integrated Design Tools, M5) was used to obtain bubble images, which were recorded at 350 mm above the nozzle tip. The bubble velocities reached the terminal velocities at this elevation. All the bubbles in the experiments rose rectilinearly without any shape oscillation and had axisymmetric shapes. The sphere-volume-equivalent diameter, d, the terminal velocity, V_T, and E were calculated using an image processing method [5]. The spatial resolution of images was 0.012 mm/pixel.

The C_D of bubbles were evaluated based on the balance between the drag and buoyant forces:

$$C_D=\frac{4(\rho_L-\rho_G)gd}{3\rho_L V_\mathrm{T}^2} \tag{2.2}$$

The bubble Reynolds number, Re, was calculated using the V_T data. The uncertainties estimated at 95% confidence were 0.01, 1.3, 2.0, 1.7, 2.7 and 0.91% for ρ, μ, σ, d, E and V_T respectively.

Triton X-100, 1-octanol, 1-decanol and sodium dodecyl sulfate (SDS) were used for surfactant. Triton X-100 and SDS are non-ionic surfactant and anionic surfactant, respectively, and have often been used in studies on surfactant effects in interfacial flows. The alcohols, i.e. 1-octanol and 1-decanol, accumulate at the gas-liquid interface and serves as surfactant. The σ decreases as the surfactant accumulates at the interface. The surfactant concentrations, C, in the liquid phase and the surface tension, σ_{eq}, measured at the adsorption-desorption equilibrium at a stationary interface are shown in **Table 2.2**. Hereafter the subscripts, T, O, DE and S, will be used for C of Triton X-100, 1-octanol, 1-decanol and SDS, respectively.

Table 2.2 Surface tensions, σ_{eq} [mN/m], at adsorption-desorption equilibrium

	Kind of surfactant and concentration C [mol/m^3]					
	Triton	Triton	Octanol	Octanol	Decanol	SDS
log$M$(σ_{eq})	0.10	0.20	2.39	3.25	0.16	5,12
−8.0	42	36	41	38	49	38
−6.7	44	38	44	39	49	40
−3.9	47	43	49	46	58	40

*C of SDS = 5 mol/m^3 at log$M$ = −8.0 and −6.7, whereas 12 mol/m^3 at log$M$ = −3.9

2.3 Discussion

2.3.1 Effects of Surfactant on C_D

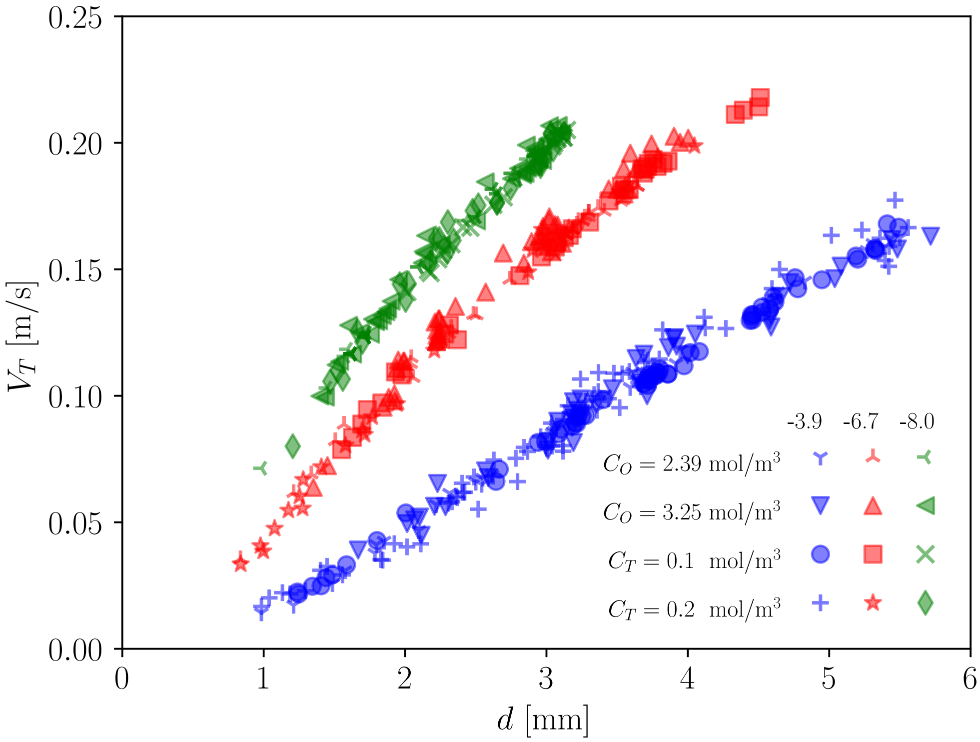

Fig. 2.1 Terminal velocities of contaminated bubbles [1]

Fig. 2.1 shows V_T of bubbles contaminated with Triton X-100 and 1-octanol. At each Morton number, the data almost lie on single curves. The 1-decanol and SDS data are also on the same curves (plots are omitted to avoid the figure to be too complex). Therefore bubbles are fully contaminated and V_T of fully-contaminated bubbles are almost independent of the kind of surfactant.

Fig. 2.2 (a), (b) and (c) show C_D. The presence of surfactant makes C_D larger than that of clean bubbles (Eq. (1.7) represented by dashed lines). The dependence of C_D on the kind of surfactant is weak.

2.3.2 Applicability of Available Drag Correlations

As discussed above, the presence of surfactant increases C_D and C_D of fully contaminated ellipsoidal bubbles do not depend on the kind of surfactant. The V_T of bubbles calculated using the Shiller-Naumann correlation, Eq. (1.7), however deviates from the data as shown in **Fig. 2.3** (dashed lines) as d increases, in other words, as E becomes small (**Fig. 2.4**). Only bubbles for d less than about 1 mm have E close to unity and the increase in d decreases E down to 0.6 at the upper limit of the present d range. It is therefore obvious that the effects of the shape deformation must be considered to obtain better evaluations of C_D of ellipsoidal bubbles.

The drag correlation, Eq. (1.9), proposed by Milizer et al.[3] is applicable to ellipsoidal solid particles for $1 < Re_S < 200$ and $0.5 \leq E \leq 2$, which covers the present experimental range of Re and E. An aspect ratio correlation is required when evaluating V_T of bubbles with the Milizer correlation. The following E correlation [5] is therefore used for calculating E:

(2.3)

where Eo is the Eötvös number defined by

$$Eo=\frac{(\rho_L\text{-}\rho_G)gd^2}{\sigma} \tag{2.4}$$

As shown in **Fig. 2.4**, Eq. (2.3) agrees well with the measured E, where the mean σ_{eq} for all the kinds of surfactant at each M were used for Eo.

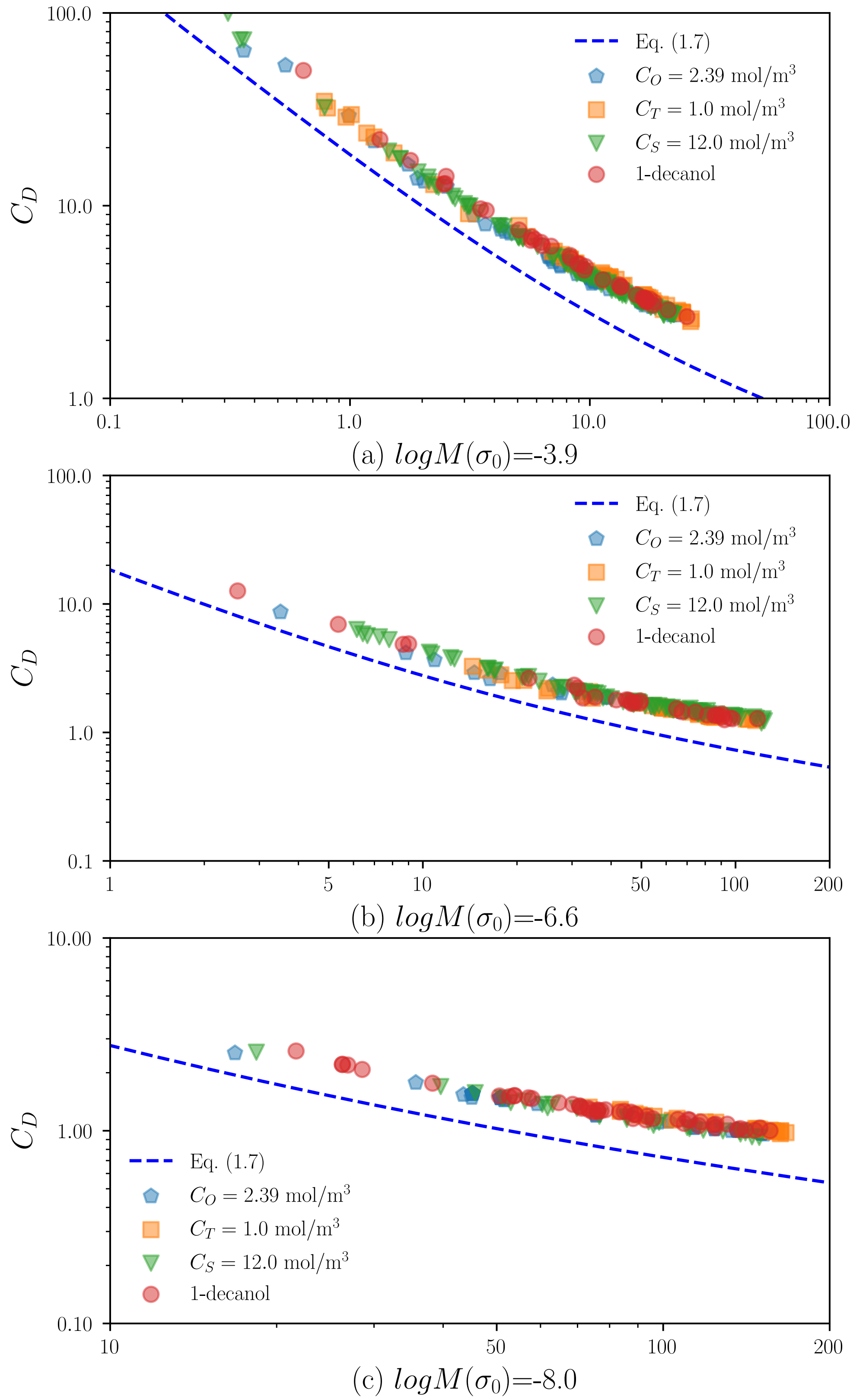

Fig. 2.2 Drag coefficients of bubbles fully-contaminated with Triton X-100, 1-octanol, 1-decanol and SDS

The V_T calculated using the Milizer correlation is compared with the data in **Fig. 2.3** (solid lines). The correlation does not give good evaluations at large d even with the shape-deformation effect multiplier, implying that the increase in d prevents the bubble interface from becoming perfectly no-slip and/or the slight break of the fore-aft symmetry of the bubble shape [1] may affect C_D.

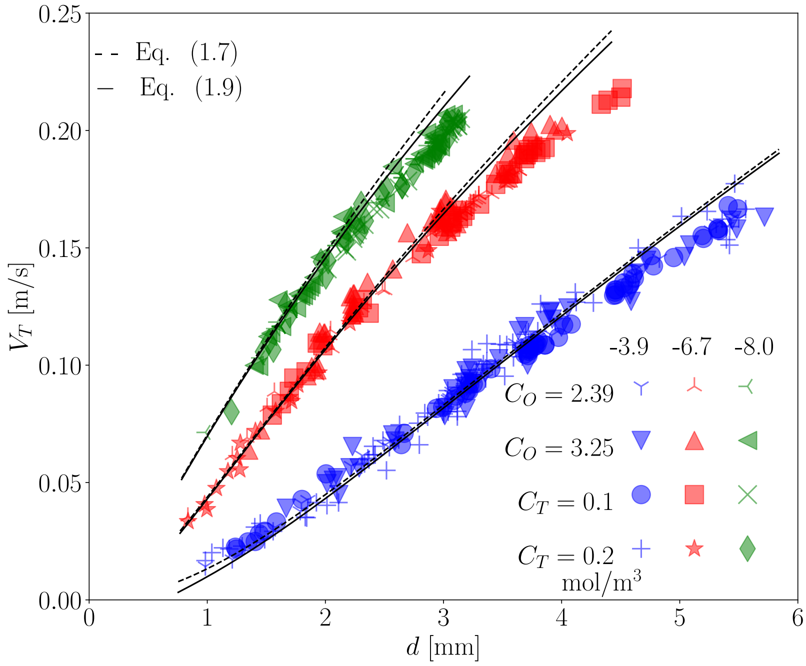

Fig. 2.3 Comparison between available C_D correlations and V_T data

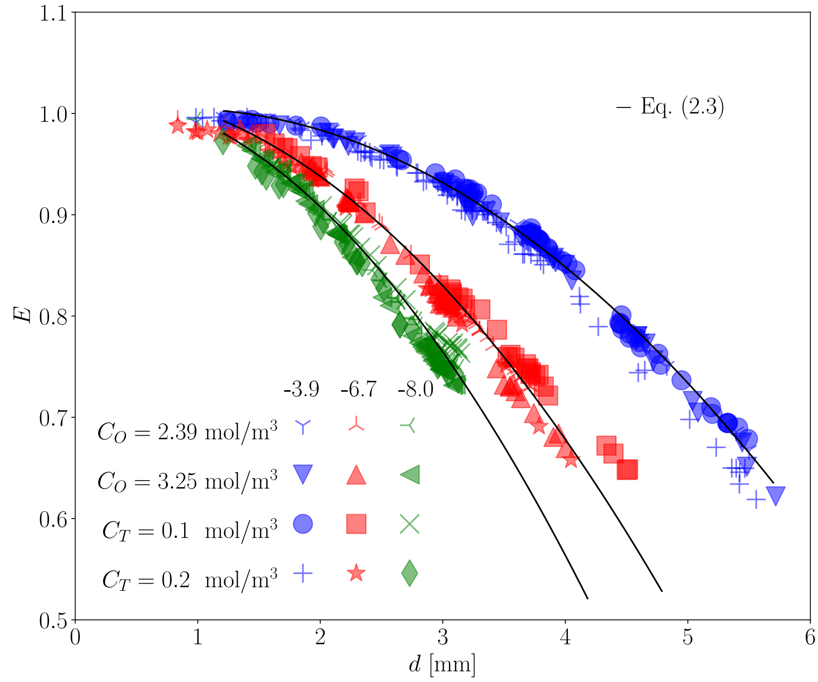

Fig. 2.4 Aspect ratios, E, of fully-contaminated bubbles

2.3.3 Drag Correlation for Contaminated Bubbles

Fig. 2.5 shows $\psi = C_D/C_D^S - 1$ evaluated using the experimental data to consider an appropriate expression for C_D, where C_D^S is the Stokes drag coefficient for a solid sphere given by

$$C_D^S = \frac{24}{Re} \tag{2.5}$$

The factor, $0.15Re^{0.687}$, the Schiller-Naumann correlation is also plotted. The monotonic increase in ψ with respect to Re supports that the Schiller-Naumann multiplier is reasonable. However the large differences between $0.15Re^{0.687}$ and the data clearly show that consideration of Re only is insufficient to correlate C_D.

As discussed in the previous section, C_D of ellipsoidal bubbles in fully contaminated systems do not depend on the kind of surfactant under the fully-contaminated condition, and therefore, C_D may be expressed in terms of Re and E. The Schiller-Naumann correlation, Eq. (1.7), can give good evaluations for bubbles with small shape deformation. The functional form of Eq. (1.7) is therefore employed as the basis of a new C_D correlation. Hence

$$C_D = C_D^S[1+\psi(Re,E)] \tag{2.6}$$

with the Schiller-Naumann multiplier,

$$\psi(Re,E)=0.15Re^{0.687}f(E,Re) \tag{2.7}$$

where the factor, $0.15Re^{0.687}$, is the inertial effect multiplier for spherical bubbles and the function, $f(E, Re)$, is a multiplier for the shape-deformation effect and a correction for inertial effect on ellipsoidal bubbles.

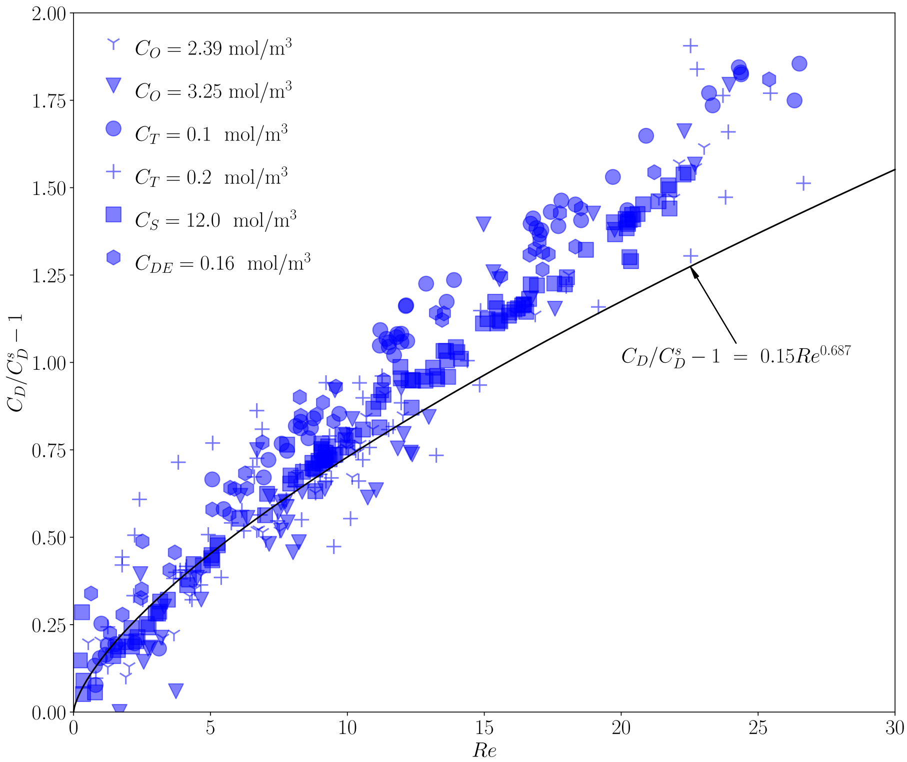

(a) $\log M(\sigma_0) = -3.9$

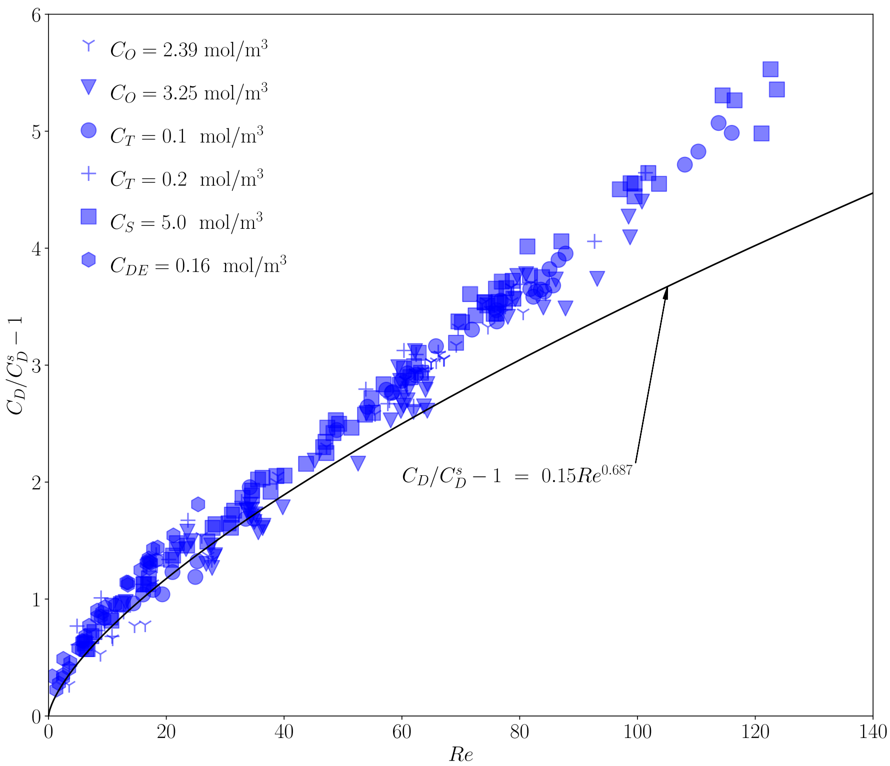

(b) $\log M(\sigma_0) = -6.7$

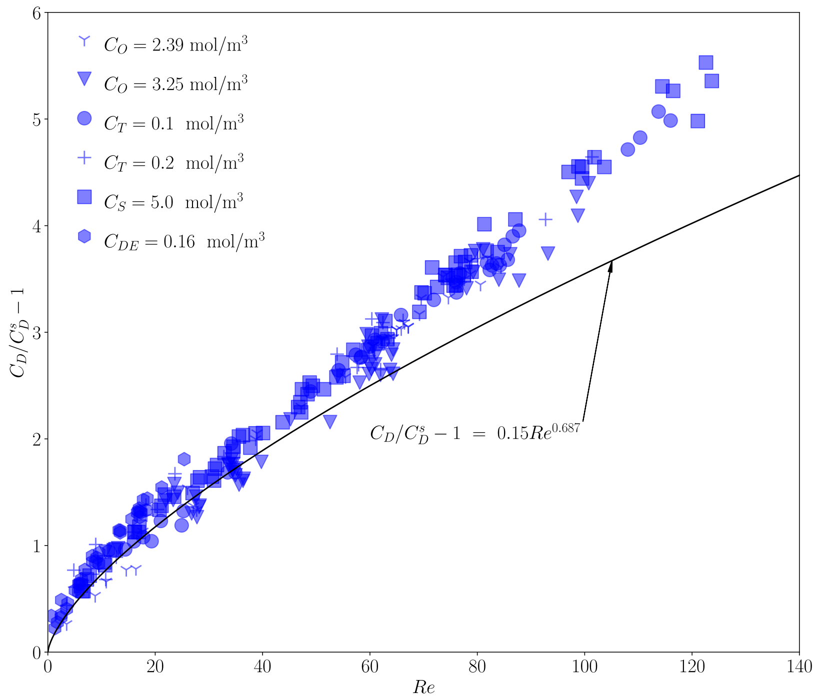

(c) log$M(\sigma_0) = -8.0$

Fig. 2.5 Factor $\psi = C_D/C_D^S - 1$ representing inertia and shape deformation effects on C_D

Fig. 2.6 shows f evaluated using the experimental data. The f decreases with increasing E. The scatter is large for $E > 0.9$ because of the small errors in measured d due to low spatial resolution for small bubbles. It would be reasonable to assume $f(1, Re) = 1$, since C_D of such spherical bubbles can be well evaluated with Eq. (1.7). The dependence of f on Re is not significant as shown in **Fig. 2.6**, so that f can be expressed as $f(E) = 1/E^{\alpha}$ to assure $f(1) = 1$. Fitting this functional form to the data yields $\alpha = 0.48$. Hence

$$\psi(Re, E) = \frac{0.15Re^{0.687}}{E^{0.48}} \tag{2.8}$$

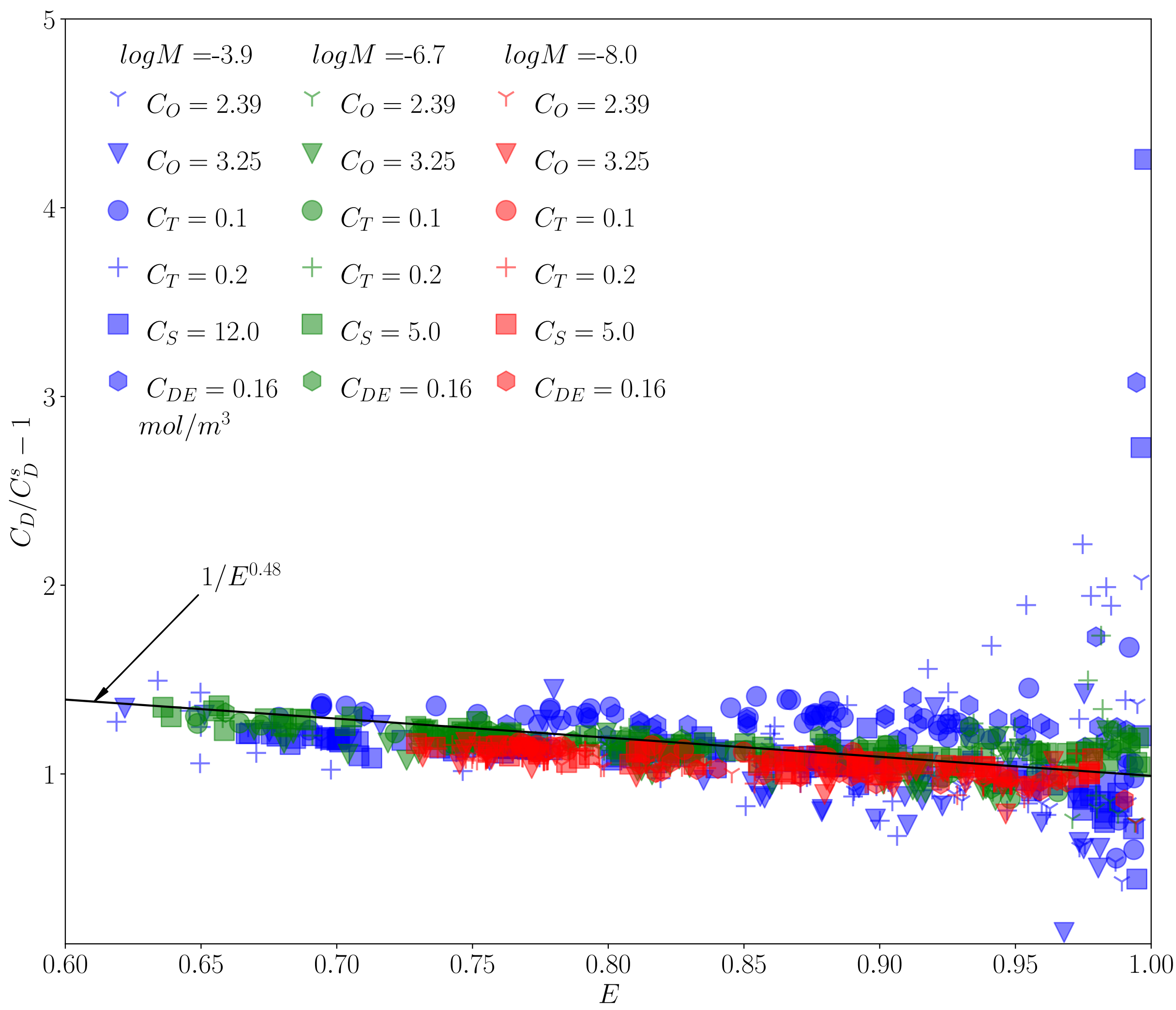

Fig. 2.6 Dependence of $C_D/C_D^S - 1$ on E

Figure 2.7 shows the data of $C_D/C_D^S - 1$ plotted against $0.15Re^{0.687}/E^{0.48}$. Eq. (2.8) agrees well with the data. The C_D correlation for fully-contaminated bubbles is thus given by

$$C_D = \frac{24}{Re}\left[1 + \frac{0.15Re^{0.687}}{E^{0.48}}\right] \tag{2.9}$$

It should be noted that the coefficients 0.15 and 0.687 do not change so much even if the constants, a, b and α, in the functional form, $C_D = C_D^S[1 + aRe^b/E^\alpha]$ is fitted to the data using the least-square method.

The V_T calculated using Eq. (2.9) is shown in **Fig. 2.8**, where Eq. (2.3) is used for evaluating E. The agreements with the data are good in the whole range of d and the accuracy is much better than Eqs. (1.7) and (1.9) especially at large d. The root mean square errors are 0.00297 m/s, 0.00849 m/s and 0.00136 m/s for Eqs. (1.7), (1.9) and (2.9), respectively. Thus the simple and accurate C_D correlation for fully-contaminated bubbles has been developed by accounting for the shape deformation effect.

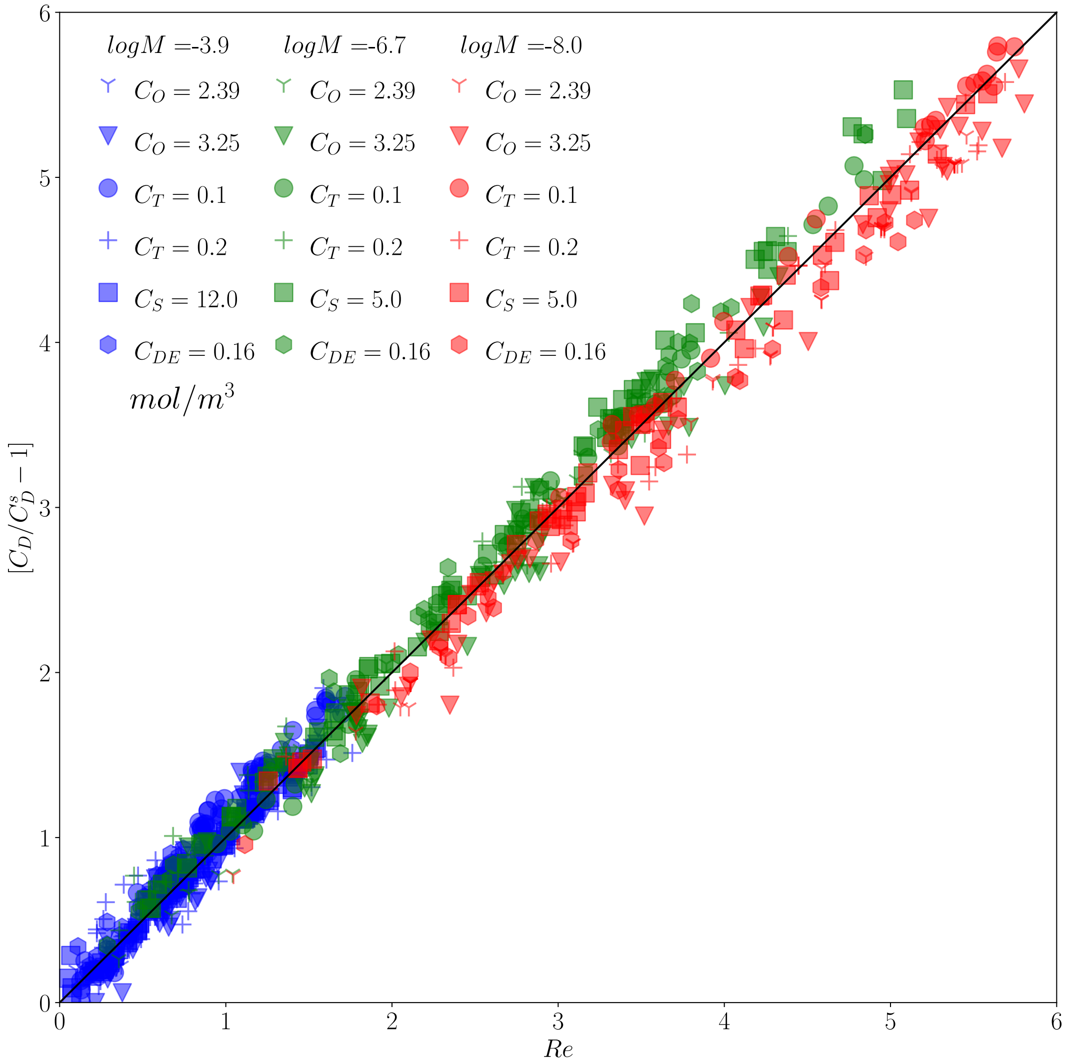

Fig. 2.7 Correlating inertia and deformation effect factors using *Re* and *E*

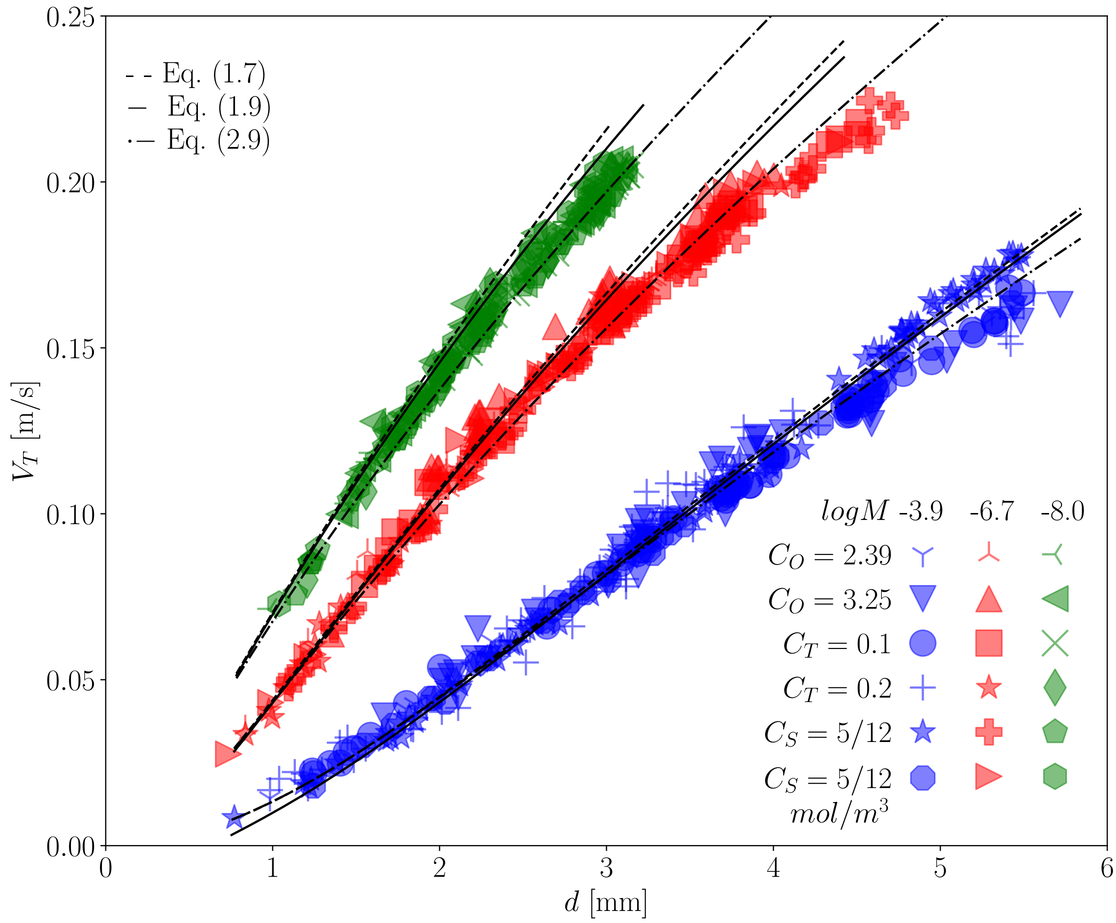

Fig. 2.8 Bubble velocities calculated using proposed C_D correlation, Eq. (2.9)

2.3.4 Drag correlation for clean bubbles

As discussed in Sec. 1.2, the C_D correlation proposed by Reastello et al. [4] is complicated although it gives acceptable evaluation of V_T for ellipsoidal bubbles in clean systems for a relatively wide range of M [1]. In the following a simpler C_D correlation for clean ellipsoidal bubbles will be developed.

By setting $E = 1$, the Rastello correlation reduces to

$$C_D=\frac{16}{Re}\left[1+[\frac{8}{Re}+\frac{1}{2}(1+\frac{3.315}{Re^{1/2}})]^{-1}\right] \tag{2.10}$$

which corresponds to Mei's C_D correlation for spherical bubbles [6]. The inertial-effect factors in Eq. (2.10) and Eq. (1.8) can be written in the same form, i.e.

$$C_D = C_D[1+\psi'(Re)] \tag{2.11}$$

By referring the shape-deformation effect in Eq. (2.9) for fully-contaminated bubbles, the aspect ratio can be added into Eq. (2.11) as an independent variable:

$$C_D = C_D[1+\psi''(Re,E)] \tag{2.12}$$

Using the Schiller-Naumann type inertial effect multiplier for the Re dependence and assuming that ψ'' is inversely proportional to E^{α} as in Eq. (2.8) yields

$$\psi''(Re,E) = \frac{aRe^{b}}{E^{\alpha}} \tag{2.13}$$

Fitting Eq. (2.12) to the clean bubble data in Aoyama et al. [1],[5] ($-8.0 < \log M \leq -3.2$) yields $a = 0.25$, $b = 0.32$ and $\alpha = 1.9$. The ψ'' with these constants agrees well with the data as shown in **Fig. 2.9**. The correlation of C_D is obtained as:

$$C_D = \frac{16}{Re}\left[1+\frac{0.25Re^{0.32}}{E^{1.9}}\right] \tag{2.14}$$

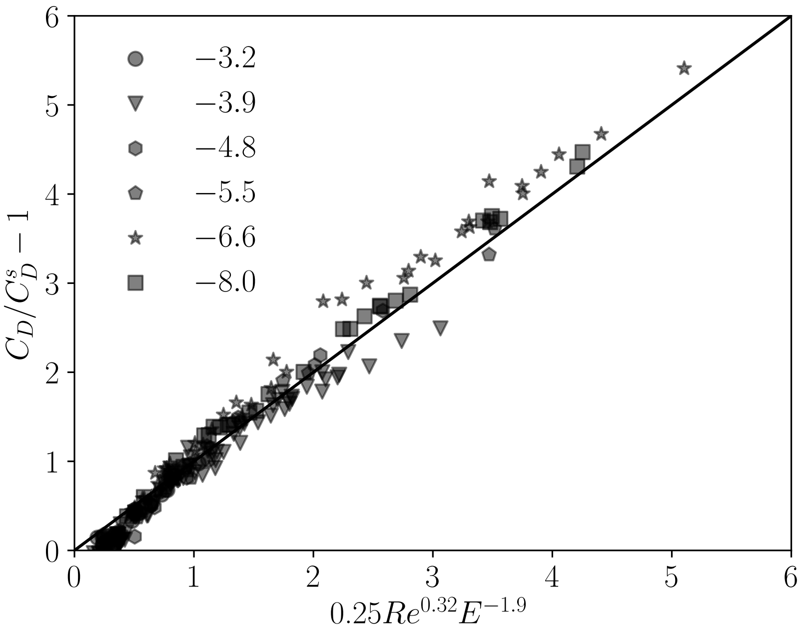

Fig. 2.9 Inertia and deformation effect factor, $\psi''(Re, E)$, for clean bubbles

Fig. 2.10 shows comparisons between the clean bubble data and Eq. (2.14) and (1.12). The E in the correlations were evaluated using the following aspect ratio correlation for clean ellipsoidal bubbles:

$$E = \frac{1}{[1+0.016Eo^{1.12}Re]^{0.388}} \quad [1] \tag{2.15}$$

Note that Rastello et al. [4] did not give any E correlation although Eq. (1.12) requires E. The comparisons show that these correlations agree with the data.

The V_T data of Sugihara et al. [7] and those given in Liu et al. [8] are compared with the correlations in **Fig. 2.11** to examine the applicability of Eq. (2.14) to a wider range of M. The $\log M$ in the former is −11 and those in the latter are −0.60 and 6.3. Numerical data at $\log M =$ −3.4 and −2.3 obtained using an interface tracking method are also shown (see Sec. 2.4). The comparisons show that the proposed correlation is also applicable to this range of M. The accuracy of the proposed correlation is almost the same as that of the elaborate correlation, Eq.

(1.12), i.e. the root mean square errors are 0.00189 m/s and 0.00237 m/s for Eqs. (2.14) and (1.12), respectively.

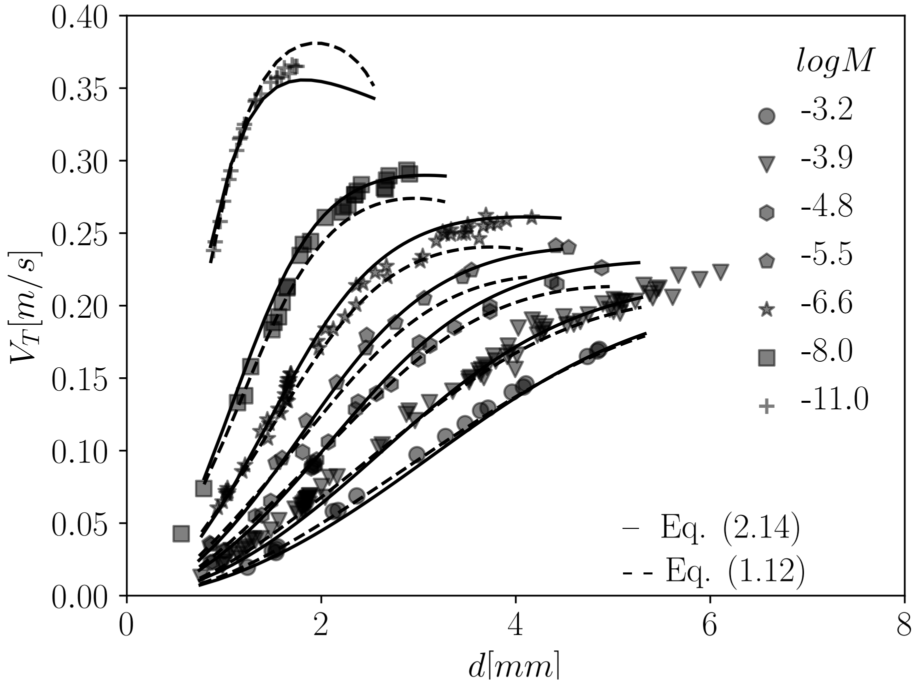

Fig. 2.10 Comparison between calculated terminal velocities and data [1]

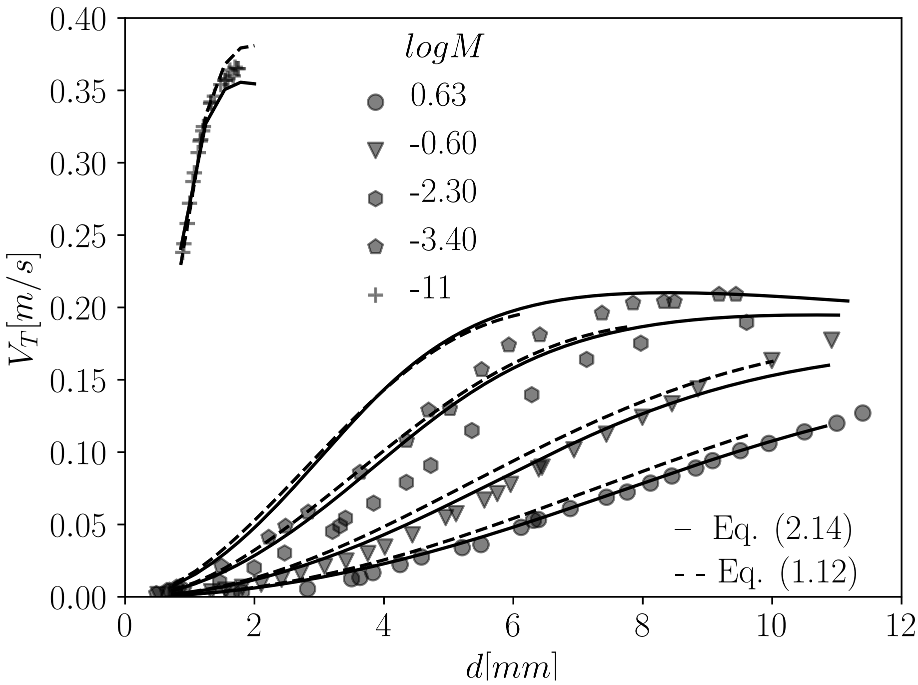

Fig. 2.11 Comparison between Eq. (2.14) and (1.12) and V_T data for a wider range of M (The data are quoted from Sugihara et al. [7] and Liu et al. [8] and numerical data given in Sec. 2.4 are also used.)

2.4 Numerical simulation of bubbles in clean systems

2.4.1 Previous data

In Sec. 2.3, the velocity data of clean bubbles [1] is used to validate the applicability of Eq. (2.14). A part of the experimental data obtained by Liu et al. [8] was then used to validate the correlation for more viscous liquids. They gave V_T data at log$M$ = 0.63, −0.60, −2.3 and −3.4 (see **Table 2.3**), which were referred to as Case S1, S2, S3 and the condition of S4 lies between those of log$M$ = −3.2 and −3.9 in Aoyama et al. [1]. However, it can be noticed that the dependence of V_T on log$M$ in the Liu data and ours is not systematic (**Fig. 2.12**). In addition, the Rastello correlation gave good evaluations for S1 and S2, whereas the deviations from the data of S3 and S4 were very large (**Fig. 2.13**). Hence it should be avoided to directly use the Liu data for validation of the drag correlations. Instead, interface tracking simulations are carried for the experimental conditions in Liu et al.. to obtain velocity database for validation of Eq. (2.14).

Table 2.3 liquid properties in Liu's experiments

Case	log$M(\sigma_0)$	ρ_L [kg/m^3]	μ_L [mPa·s]	σ_0 [mN/m]
S1	0.63	1246	622	65
S2	−0.60	1236	306	65
S3	−2.3	1220	115	66
S4	−3.4	1207	63	67

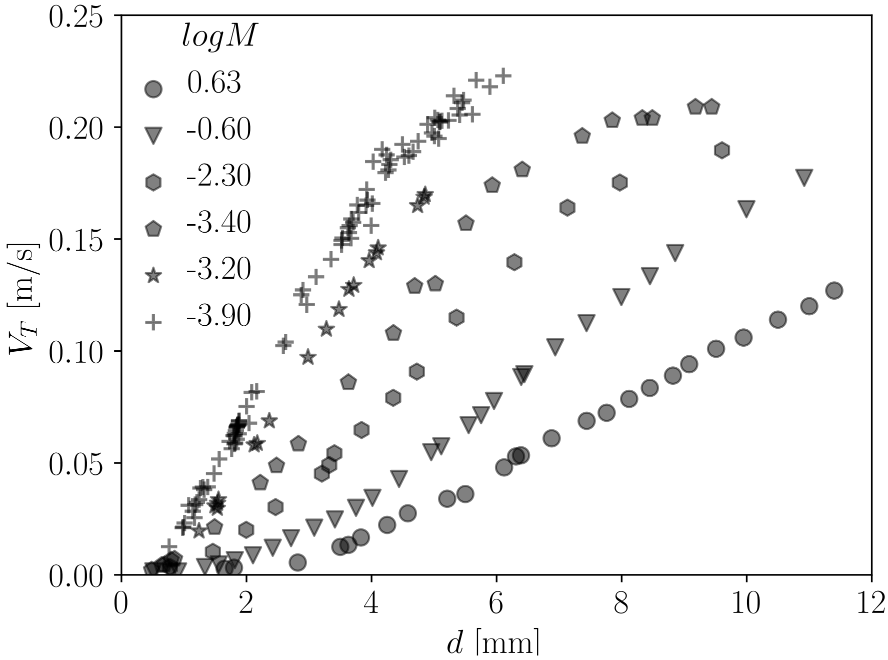

Fig. 2.12 Comparisons of V_T data between Liu's experiment and Aoyama's experiment

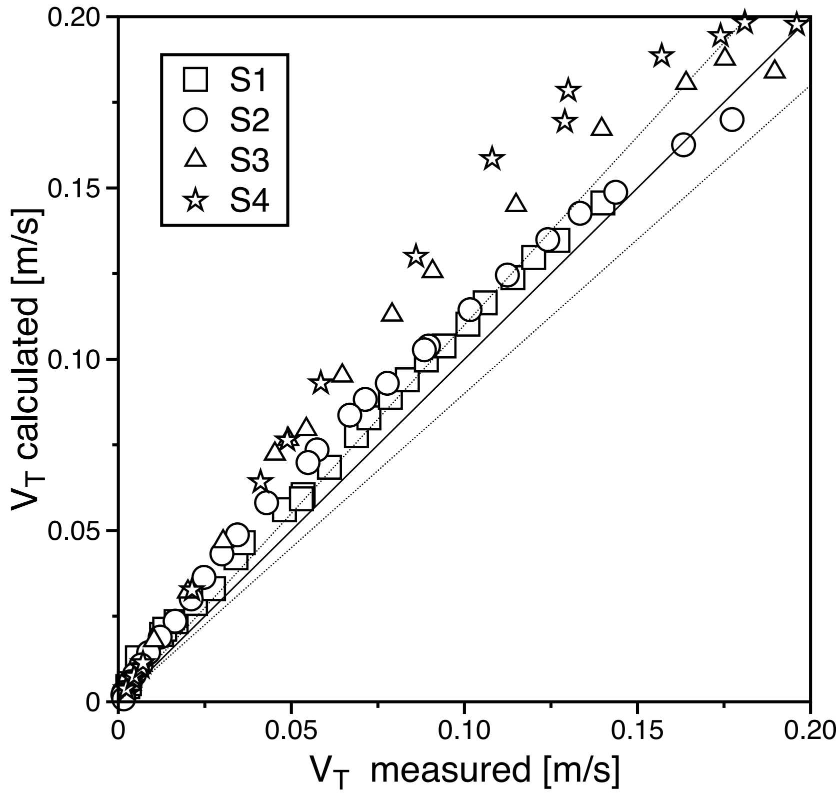

Fig. 2.13 Comparisons between Liu's V_T data and Rastello correlation, Eq. (2.7)

2.4.2 Governing equations

Although the Liu experiments dealt with large bubbles exhibiting some wobbling motion, only bubbles having axisymmetric shapes and rectilinear rise paths were simulated in the present study. The two-dimensional (r, z) cylindrical coordinate system was therefore used. The continuity equation is given by

$$\frac{1}{r}\frac{\partial r u_r}{\partial r} + \frac{\partial u_z}{\partial z} = 0 \qquad (2.16)$$

where u_r and u_z are the velocity components in the r and z directions, respectively. The Navier-Stokes equation for Newtonian fluids based on the one-fluid formulation is given by

$$\frac{\partial u_r}{\partial t} + u_r\frac{\partial u_r}{\partial r} + u_z\frac{\partial u_r}{\partial z} = -\frac{1}{\rho}\frac{\partial P}{\partial r} + \frac{1}{\rho}\left[D_r + \frac{\partial \mu}{\partial r}\frac{\partial u_r}{\partial r} + \frac{\partial \mu}{\partial z}\frac{\partial u_z}{\partial r}\right] - \frac{\sigma\kappa n_r \delta}{\rho} \qquad (2.17)$$

$$\frac{\partial u_z}{\partial t} + u_r\frac{\partial u_z}{\partial r} + u_z\frac{\partial u_z}{\partial z} = -\frac{1}{\rho}\frac{\partial P}{\partial z} + \frac{1}{\rho}\left[D_z + \frac{\partial \mu}{\partial r}\frac{\partial u_r}{\partial z} + \frac{\partial \mu}{\partial z}\frac{\partial u_z}{\partial z}\right] - \frac{\sigma\kappa n_z \delta}{\rho} \qquad (2.18)$$

where t is the time, P the pressure, ρ the mixture density, μ the mixture viscosity, κ the interface curvature, $\boldsymbol{n}_I = (n_r, n_z)$ the unit normal to the interface, δ the delta function, and

$$D_r = \frac{1}{r}\frac{\partial}{\partial r}\left(r\mu\frac{\partial u_r}{\partial r}\right) + \frac{\partial}{\partial z}\left(\mu\frac{\partial u_r}{\partial z}\right) + \mu\frac{u_r}{r^2} \qquad (2.19)$$

$$D_z = \frac{1}{r}\frac{\partial}{\partial r}\left(r\mu\frac{\partial u_z}{\partial r}\right) + \frac{\partial}{\partial z}\left(\mu\frac{\partial u_z}{\partial z}\right) \qquad (2.20)$$

The level set method [9],[10] was used to track the gas-liquid interface. The interface is given by the zero-level set, i.e. $S = 0$, where S is the signed-distance function and advected using

$$\frac{\partial S}{\partial t} + u_r\frac{\partial S}{\partial r} + u_z\frac{\partial S}{\partial z} = 0 \qquad (2.21)$$

2.4.3 Numerical method and conditions

The fractional step method was used to couple the continuity and the Navier-Stokes equation. The advection and diffusion terms of the Navier-Stokes equation were discretized using the 2nd-order ENO and the 2nd-order centered difference schemes, respectively. The 2nd-order Runge-Kutta and Crank-Nicolson schemes were used for these terms. The staggered variable arrangement was used. The $\boldsymbol{n}_I$ and κ were evaluated using the 2nd-order centered difference scheme.

Eq. (2.20) was solved using the 2nd-order TVD Runge-Kutta [11] and ENO schemes. The property, $|\nabla S| = 1$, of the distance function is deteriorated after advection. Therefore the following re-initialization equation was solved at each time step:

$$\frac{\partial S}{\partial \tau} = \mathrm{sign}(S_0)(1 - |\nabla S|) \tag{2.22}$$

where τ is the pseudo time, sign the smoothed sign function, and S_0 the level set function after solving Eq. (2.20). The Runge-Kutta and ENO schemes were used also for Eq. (2.21). The 2nd-order interface fixing technique was used to mitigate the volume loss during the re-initialization process [11]. Since the volume conservation could be insufficient even with the interface fixing, a global volume correction was applied at each time step [12]. Detailed descriptions of the numerical method can be found in Hayashi and Tomiyama [13].

Fig. 2.14 shows the computational domain, whose width and height are $4d$ and $8d$, respectively. The initial bubble shape was sphere and the bubble was placed in the uniform-square cell region, in which the computational cell width was d/N, where $N = 40$. Non-uniform rectangular cells were used in the other region to save the computational cost. The left boundary was axisymmetric, the top boundary was uniform inflow, and the right and bottom boundaries were continuous outflow. For a grid convergence test, N was changed from 20 to 50, and $N = 40$ was confirmed to be large enough to obtain well-converged V_T. The fluid properties given in **Table 2.3** were used.

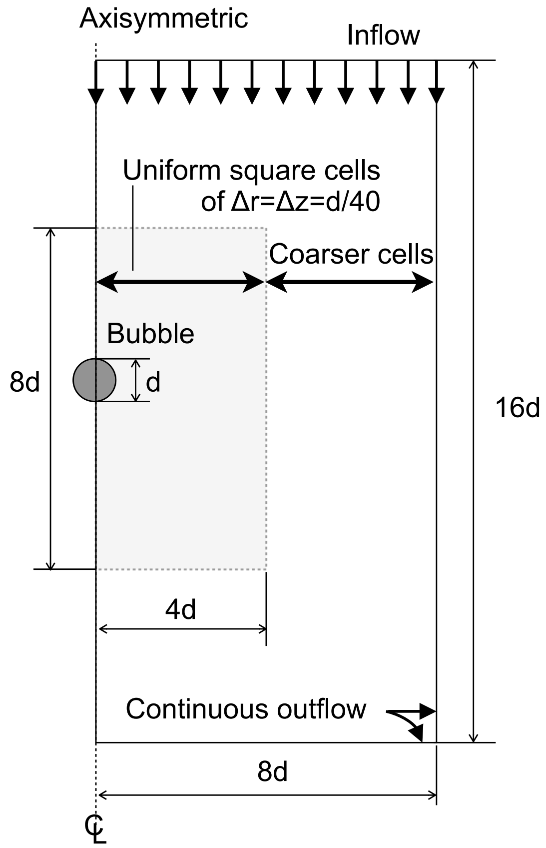

Fig. 2.14 Computational domain

2.4.4 Comparison between predictions and experimental data

Fig. 2.15 shows comparisons between the numerical predictions of V_T and Liu's experimental data. The predictions agree with the data of S1 and S2. However the predictions largely differ from the data of S3 and S4. The V_T calculated using Eqs. (2.14) and (1.12) are also plotted as the solid and dotted lines, respectively. The agreements between the predictions and the correlations are reasonable in all the cases. As shown in **Fig. 2.15**, the correlations agree well with the data at $\log M = -3.9$ and -3.2 in Aoyama et al. [1], which are close to S4 ($\log M = -3.4$). It can therefore be concluded that Liu's data of S3 and S4 include some errors, whereas those of S1 and S2 are available for validation of drag correlations.

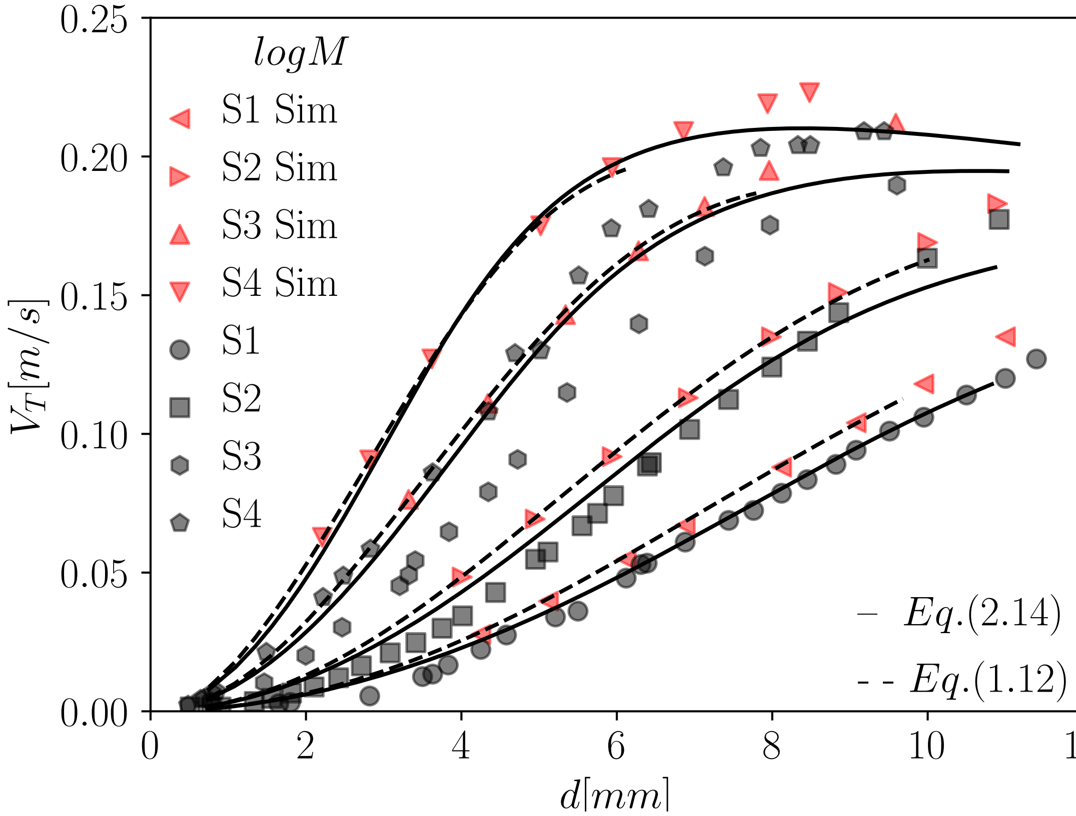

Fig. 2.15 Comparison between predictions of V_T (labeled as Sim) and experimental data [8]

2.5 Summary

Effects of the aspect ratio on the drag coefficients, C_D, of single ellipsoidal bubbles in fully-contaminated systems are investigated to develop a C_D correlation accounting for bubble shape. For this purpose the experimental data of the bubble terminal velocity and bubble aspect ratio, E, obtained by Aoyama et al. [1] were used. Triton X-100, 1-octanol, 1-decanol and SDS were used for surfactant in the experiments. A C_D correlation for clean ellipsoidal bubbles was also developed. As a result, the following conclusions were obtained:

(1) The kind of surfactant has little influence on C_D of fully-contaminated bubbles, and therefore, C_D can be correlated in terms of the bubble Reynolds number Re and E.

(2) The following simple drag correlation was proposed for fully-contaminated ellipsoidal bubbles rectilinearly rising through stagnant liquids:

$$C_D=\frac{24}{Re}\left[1+\frac{0.15Re^{0.687}}{E^{0.48}}\right]$$

which gives good evaluation of the terminal velocity V_T for $-8.0 \le \log M \le -3.2$, $0.53 \le Re \le 166$ and $0.12 \le Eo \le 8.2$.

(3) The C_D of clean ellipsoidal bubbles in stagnant liquids was well correlated using the same functional form, i.e.

$$C_D=\frac{16}{Re}\left[1+\frac{0.25Re^{0.32}}{E^{1.9}}\right]$$

which gives good predictions of V_T for $-11 \le \log M \le 0.63$, $3.2\text{x}10^{-3} \le Re \le 720$ and $0.042 \le Eo \le 29$.

References

[1] Aoyama, S., Hayashi K., Hosokawa, S., Tomiyama, A., 2016. Shapes of Ellipsoidal Bubbles in Infinite Stagnant Liquids, International Journal of Multiphase Flow, 79, 23-30

[2] Tomiyama, A., Kataoka, I., Zun, I., Sakaguchi, T., 1998. Drag Coefficients of Single Bubbles under Normal and Micro Gravity Conditions, JSME International, 41(2), 472-479.

[3] Militzer, J., Kan, J. M., Hamdullahpur, F., Amyotte, P. R., Al Taweel, A. M., 1989. Drag Coefficient for Axisymmetric Flow around Individual Spheroidal Particles, Powder technology, 57, 193-195.

[4] Rastello, M., Marié, J.-L., Lance, M., 2011. Drag and Lift Forces on Clean Spherical and Ellipsoidal Bubbles in a Solid-Body Rotating Flow, Journal of Fluid Mechanics, 682, 434-459.

[5] Aoyama, S., Hayashi, K., Hosokawa, S., Tomiyama, A., 2018. Shapes of Single Bubbles in Infinite Stagnant Liquids Contaminated with Surfactant, Experimental Thermal and Fluid Science, 96, 460-469.

[6] Mei, R., Kalusner, J. F., Lawrence, C. J., 1994. A Note on the History Force on a Spherical Bubble at Finite Reynolds Number, Physics of Fluids, 6, 418–420.

[7] Sugihara, K., Sanada, T., Shirota, M., Watanabe, M., 2007. Behavior of Single Rising Bubbles in Superpurified Water, Kagaku-Kogaku Ronbun-shu, 5, 402-408.

[8] Liu, L., Yan, H., Zhao, G., Zhuang, J., 2016. Experimental Studies on the Terminal Velocity of Air Bubbles in Water and Glycerol Aqueous Solution, Experimental Thermal and Fluid Science, 78, 254–265.

[9] Sussman, M., Smereka, P., Osher, S., 1994. A Level Set Approach for Computing Solutions to Incompressible Two-Phase Flow, Journal of Computational Physics, 114, 146-159.

[10] Sussman, M., Fatemi, E., Smereka, P., Osher, S., 1998. An Improved Level Set Method for Incompressible Two-Phase Flows, Computers & Fluids, 27, 663-680.

[11] Min, C. and Gibou, F., 2007. A Second Order Accurate Level Set Method on Non-Graded Adaptive Cartesian Grids, Journal of Computational Physics, 225(1), 300-321.

[12] Meier, M., 2000. Towards a DNS of multiphase flow, Institutor Energietechnik, LA-8355, Zurich.

[13] Hayashi, K., Tomiyama, A., 2018. Interface Tracking Methods, Chapter 2 in Encyclopedia of Two-Phase Heat Transfer and Flow III, et. John R. Thome, World Scientific, Singapore.

Chapter 3

Application of deep learning to lift coefficient of clean bubbles in linear shear flow

3.1 Introduction

The artificial neural network, ANN, is expected to give good evaluations of model coefficients in the constitutive equations such as the drag and lift force, which are required in bubbly flow simulations based on the averaging models. An advantage of the ANN correlation is that it can be easily improved by a re-learning process when new experimental, numerical, and analytical data of the model coefficients are available. The ANN is trained by using the gradient descent learning. Here the NAG [Nesterov accelerated gradient] algorithm [1] is used for learning. The weight parameters are initialized using the Gaussian distribution[2]. The mean squared error is used as the loss function for evaluating the performance of the ANN. The machine learning application in this study is developed by using the following pack ages: Keras (version 2.3.1) using TensorFlow (version 2.0.0) backend, and Scikit-Learn (version 0.23.2).

3.2 Input and output layers

Multifluid models and bubble tracking methods require the lift coefficient C_L when solving the momentum equations. The coefficient depends on several quantities such as the bubble size, the instantaneous bubble and liquid velocities, and the fluid properties, i.e., the gas and liquid densities, the liquid viscosity, and the surface tension. It is possible to use these variables as the inputs of the ANN model. However, it would be better to reduce the number of input variables for making the ANN model as simple as possible. For this purpose, the relevant dimensionless groups can be used. The C_L of bubbles in linear shear flows are expected to be expressed in terms of the bubble Reynolds number Re, the Eötvös number Eo, and the dimensionless shear rate Sr [3],[4]. It has been pointed out that the bubble shape is a key parameter determining the magnitude of the negative component of the lift force acting on ellipsoidal bubbles [5],[6], and the bubble aspect ratio E has been adopted as one of the independent variables in C_L correlations [6],[7],[8],[9] though E may also be a function of *Re*, *Eo*, and *Sr*. Aoyama et al. pointed out that *E* is rarely affected by weak liquid shear, and some *E* correlations are available [10], [7], [11], [12]. Therefore, *Re*, *Eo*, *Sr*, and *E* are used as the inputs **x** in this study. The C_L is the only output of the present ANN models.

The C_L data were quoted from the literature [3], [12],[9]. The numbers of the data points and the ranges of the dimensionless groups are shown in Table 3.1, where *M* is the Morton number.

The *Re* and *Eo* range from the order of 10^{-1} to 10^3 and from 0.01 to 10, respectively. The wide ranges of these features may deteriorate the training efficiency. Therefore, log *Re* and log *Eo* are used instead of *Re* and *Eo* to put the data points into narrower variable ranges. Then, all the features are normalized by the mean and the variance of the training data.

The data for training and test are randomly selected from the database with the ratios of 0.8 and 0.2 for the former and the latter, respectively. No stratification is applied in the data extraction. The training data are used in the model development phase, and the test data are used only in the final performance test.

Table 3.1: Dimensionless groups in datasets. A: Aoyama et al. [3] (clean system), H: Hessenkemper et al. [11] (purified, deionized, tap), L: Lee and Lee [9] (contaminated). The values in the parentheses represent the number of data points in each dataset

	Re	*Eo*	*Sr*	*M*
A (562)	0.1 ~ 120	0.027 ~5.0	0.03 ~ 0.43	$2.3 \times 10^{-7} \sim 6.3 \times 10^{-4}$
H (77)	660 ~ 1520	0.68 ~ 5.8	0.018 ~ 0.075	2.6×10^{-11}
L (11)	440 ~ 7170	0.63 ~ 55	0.0044 ~ 0.024	1.4×10^{-11}

3.3 K-Folds cross validation

The performances of the ANNs of different N_n and N_l are examined by using the K-folds cross validation. The number of folds is five. The losses in the training L_t and validation L_v are averaged for the folds. Twenty percent of the training set are randomly extracted for validation in each fold. The learning rate and the momentum in NAG are 0.1 and 0.9, respectively. The batch size is set to the size of the training set.

Figure 3.1 shows the loss histories in each case. In Case (1, 10), the simplest model among the models tested, L_t steeply decreases with increasing the epoch at the early stage of the training. The decreasing rate of L_t then decreases, and L_t approaches a constant value (~ 0.006). The L_v also shows a steep reduction at the early stage. However, after 400 epochs L_v increases, which implies that the model overfits the training data. The L_v then approaches a value about ten times larger than the converged value in the training. The increase in N_l to $N_l = 2$ does not affect L_t so much. On the other hand, the overfitting is mitigated. Using (N_l , N_n) = (3, 10) makes L_t smaller, but the overfitting becomes remarkable. The L_t in Case (4, 10) is smaller than that in (2, 10), whereas L_v in the former is larger.

Table 3.2: Numbers of hidden layers N_l and neurons N_n in each hidden layer

	$N_l = 1$	2	3	4	5
$N_n = 10$	Case (1, 10)	Case (2, 10)	Case (3, 10)	Case (4, 10)	Case (5, 10)
20	Case (1, 20)	Case (2, 20)	Case (3, 20)	Case (4, 20)	Case (5, 20)
30	Case (1, 30)	Case (2, 30)	Case (3, 30)	Case (4, 30)	Case (5, 30)
40	Case (1, 40)	Case (2, 40)	Case (3, 40)	Case (4, 40)	Case (5, 40)

Table 3.3: Total numbers of parameters in ANN model. The values in the parentheses are the numbers of non-trainable parameters

	N_l=1	2	3	4	5
$N_n = 10$	101(20)	251(40)	401(60)	551(80)	701(100)
20	201(40)	701(80)	1201(120)	1701(160)	2201(200)
30	301(60)	1351(120)	2401(180)	3451(240)	4501(300)
40	401(80)	2201(160)	4001(240)	5801(320)	7601(400)

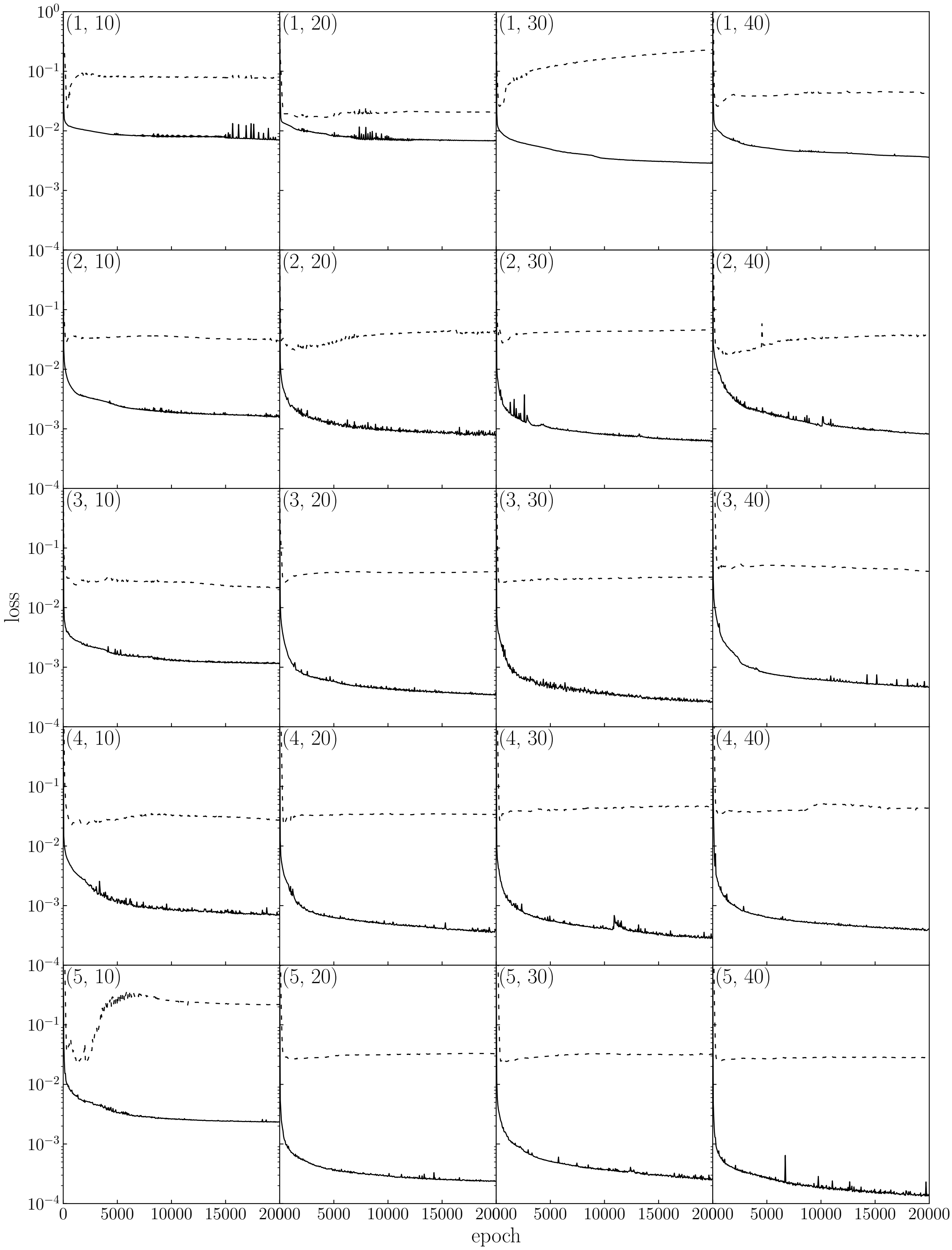

Fig. 3.1 Loss history in K-folds cross validation in each Case (Nl, Nn). Solid line: loss in training; dashed line: loss in validation.

Compared with Case (1, 10), L_t in Case (2, 10) is smaller, and the overfitting is mitigated. By increasing N_n from 10 to 20, L_t is slightly reduced, but further increase in N_n does not affect L_t so much. The L_v in the cases of $N_l = 2$ are similar.

The characteristics of Lt and Lv of $N_l = 3$ and 4 are similar to those of $N_l = 2$. Though Case (5, 10) exhibits a large deterioration of Lv due to overfitting around 5000 epochs, the other cases of $N_l = 5$ also show trends similar to those in the cases of $N_l = 3$ and 4.

In summary, Lv of $N_l = 1$ are larger than those in the other cases of $N_l > 1$, and the overfitting largely deteriorates the performance in some cases. The behaviors of Lv in the cases of $N_l > 1$ seem more sTable except for (5, 10). However, the increase in N_l from three to larger values is not effective. Although the increase in N_l decreases Lt in most cases, the orders of the magnitude of Lv are not so different. Therefore, (2, 10) or (3, 10) would be a reasonable choice as the base model to make the model as simple as possible. **Fig. 3.2** shows the loss histories of these cases up to 50,000 epochs. In both cases, overfitting does not take place even for large epochs. The latter case shows a slightly better performance than the former. In the following, the model of (3, 10) is used as the base model.

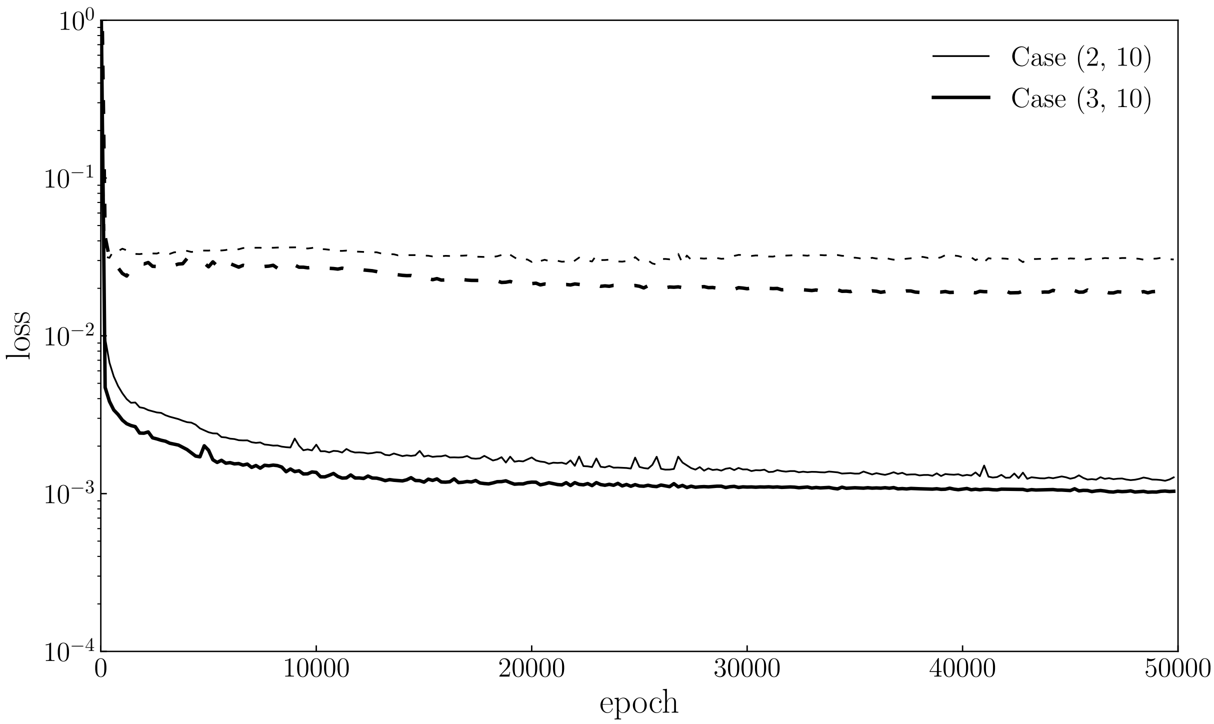

Fig. 3.2 Comparison of loss history between Cases (2, 10) and (3, 10). Solid line: loss in training; dashed line: loss in validation

3.4 Training Phase

The model of $N_n = 3$ and $N_l = 10$ is trained for the full training dataset. **Fig. 3.3** shows the loss history in the training phase of the model. The trend of the loss curve is the same as that in the cross validation, though the value of Lt of this training is somewhat smaller. Though Lt shows some oscillations, possibly due to the large learning rate, the decreasing rate in Lt is very small for epochs > 20,000. This implies that the simple model structure (3, 10) does not cause serious overfitting, even with the small size of the dataset.

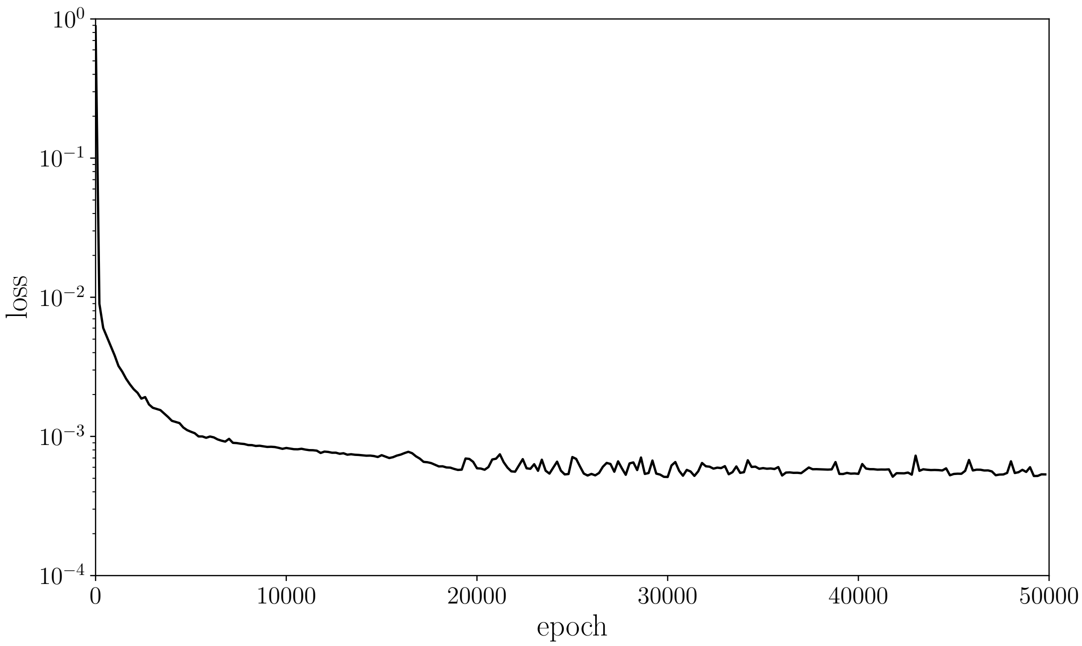

Fig. 3.3 Loss history in training phase for model of $N_l = 3$ and $N_n = 10$

Figure 3.4 shows comparisons between the predicted C_L (the closed symbols) and the training data (the open symbols) where the model parameters are for 50,000 epochs. The comparisons confirm that the present ANN model is well trained for the dataset for the wide ranges of the relevant dimensionless groups, e.g., $0.1 \leq Re \leq 7000$. Bubbles included in the dataset are either in the viscous force dominant regime or in the surface tension-inertial force dominant regime, and lift correlations may be developed using different functional forms for those regimes [7],[8]. On the other hand, the ANN correlation can cover C_L in both regimes with the single network structure. **Fig. 3.5** shows the evaluation errors in the predicted C_L, where the dotted lines represent ± 10% errors. Most data are within the 10% error range.

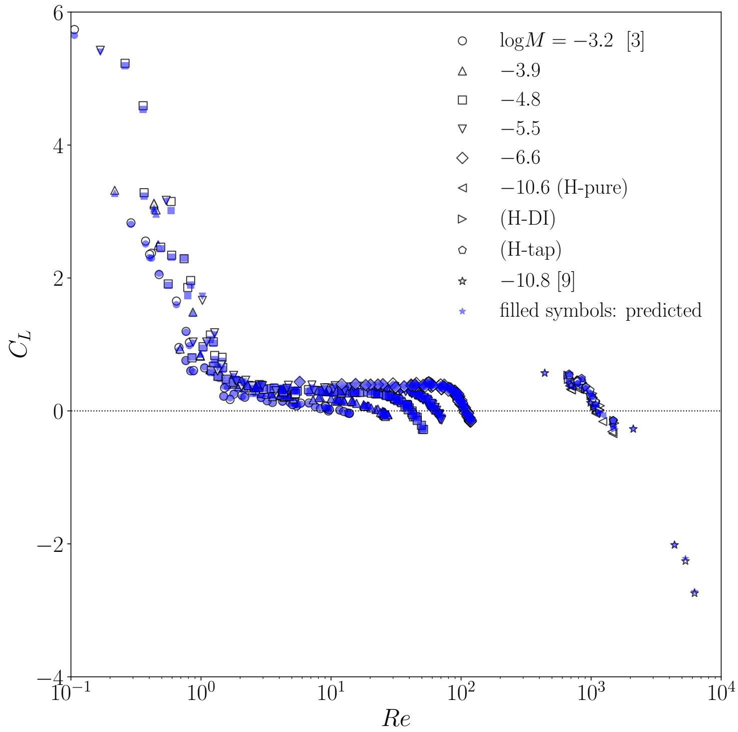

Fig. 3.4 Comparison between predicted C_L with training data (N_l = 3 and N_n = 10). Closed symbols: predicted; open symbols: training data. H-pure, H-DI, and H-tap denote bubbles in pure water, deionized water, and tap water, respectively [11].

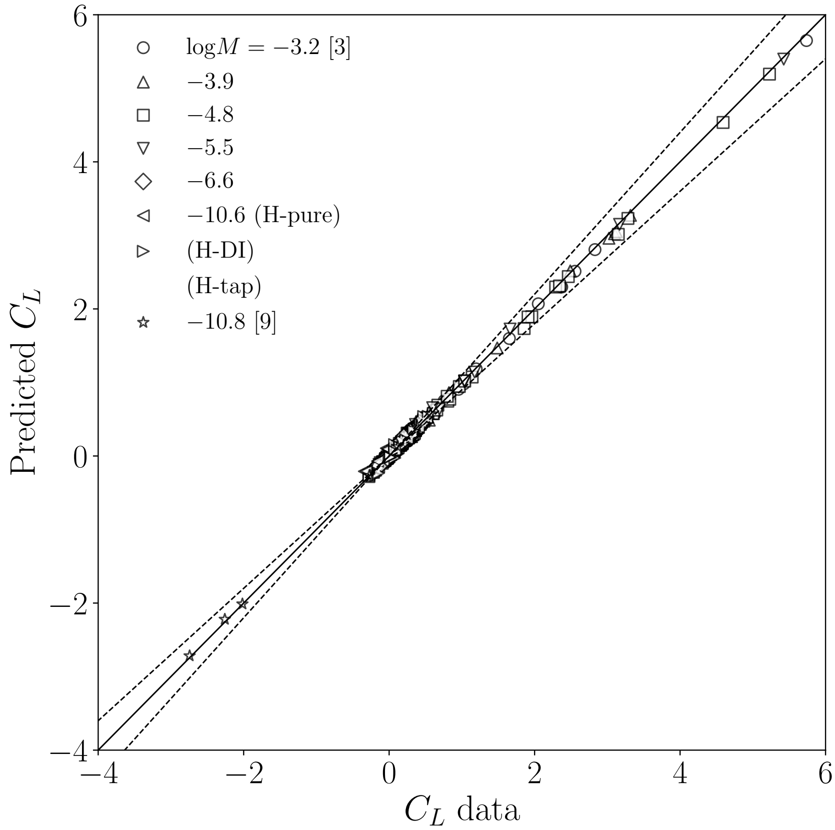

Fig 3.5 Estimation errors for training data N_l = 3 and N_n = 10

Lift curves are drawn by using the trained ANN as shown in **Fig. 3.6.** The inputs were prepared as follows:

1. Create data of *Re* for a certain range.

2. Calculate *Eo* for the *Re* data by using the following drag correlations [13], [14].

$$C_D=\frac{16}{Re}[1+\frac{0.25Re^{0.32}}{E^{1.9}}] \tag{3.1}$$

$$C_D=\frac{8}{3}\frac{E_O}{E_O+4} \tag{3.2}$$

3. Evaluate *E* by using the following shape correlations [3],[7]:

$$E=(1+0.016Eo^{1.12}Re)^{-0.388} \quad \text{(viscous force dominant regime)} \tag{3.3}$$

$$E=(1+0.62We^{0.376})^{-1} \quad \text{(surface tension} - \text{inertial force dominant regime)} \tag{3.4}$$

4. Calculate *Sr* for a given *ω*.

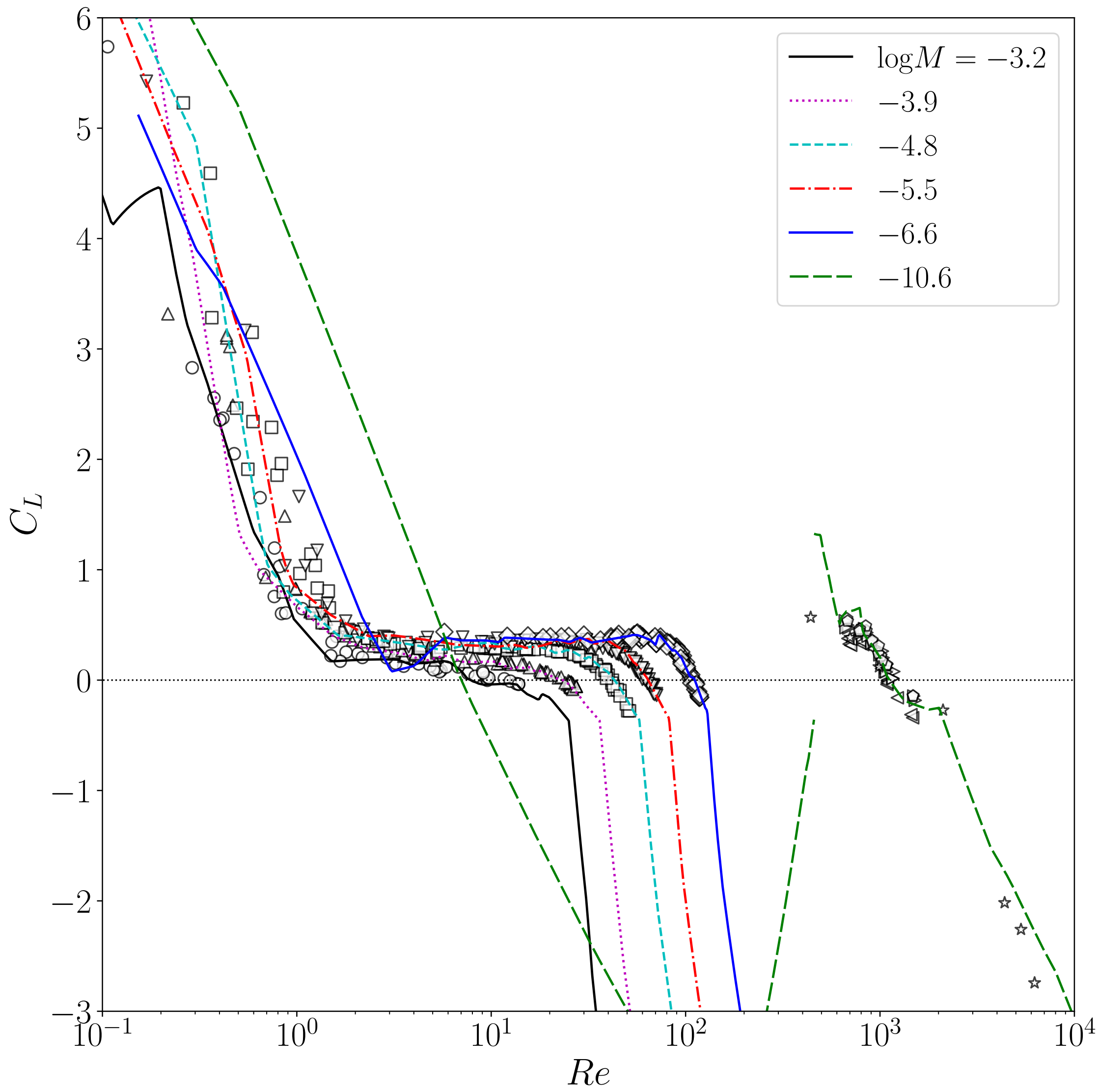

Fig. 3.6 Lift curves drawn using trained ANN model of N_l = 3 and N_n = 10. The shape correlations of Eqs. (3.3) and (3.4) are used for E. The legends of the symbols are the same as those in **Fig. 3.4**. The shear rate ω used are 3.2 and 2.3 s^{-1} for log $M \geq -6.6$ and log $M = -10.6$, respectively.

For $-5.5 \leq \log M \leq -3.9$, the agreements between the lift curves predicted by the ANN and the data are fairly good. Although the trend of the curve at log $M = -3.2$ is not good for $Re < 0.2$, the trend at larger Re is accepTable. Even though there are no data for $Re < 5.7$ at log $M = -6.6$, the ANN correlation reproduces the trend of C_L, i.e., the increase in Re largely decreases C_L. At log $M = -10.6$, the predictions are reasonable for $Re > 600$; however, at lower Re, at which no experimental data are available for training, the lift curve shows an unphysical trend.

Thus, the present ANN is capable of accurately predicting C_L for a wide range of the relevant dimensionless groups. It however requires more data to avoid causing large errors in some parameter ranges where no data are available.

3.5 Data extension using avaiable model

As discussed in the Sec. 3.4, the present ANN correlation gives relatively large errors at low Re (log $M = -3.2$, -6.6) and intermediate Re (log $M = -10.6$). Under these conditions, the bubble shape can be assumed to be almost spherical, and for spherical bubbles the following well-accepted semi-analytical correlation is available [15]:

$$C_L^S = \left(\left[C_L^{SL}\right]^2 + \left[C_L^{SH}\right]^2 \right)^{0.5} \tag{3.5}$$

where the lift coefficients of a low Reynolds number bubble C_L^{SL} [16] and a high Reynolds number bubble C_L^{SH} are given by

$$C_L^{SL} = \frac{6}{\pi^2} \frac{2.255}{\sqrt{SrRe}\left[1+0.2Re/Sr\right]^{1.5}} \tag{3.6}$$

$$C_L^{SH} = \frac{1}{2} \left(\frac{1+16/Re}{1+29/Re} \right) \tag{3.7}$$

This correlation can provide some C_L data to cover the Re ranges of inaccurate predictions. It would be worth verifying a possibility of improving the accuracy of the present ANN model by re-learning with additional data.

Whether the present ANN structure is capable of expressing Eq. (3.6) is discussed in the next. The number of the data generated for this purpose is 400. The bubble Reynolds numbers and the dimensionless shear rate for the input are randomly selected. The Eötvös numbers are determined using the following drag correlation for spherical bubbles [17]:

$$C_D=\frac{16}{Re}\left[1+\left(\frac{8}{Re}+\frac{1}{2}\left(1+\frac{3.315}{\sqrt{Re}}\right)\right)^{-1}\right] \tag{3.8}$$

Fig. 3.7 shows comparisons between the generated data and predictions using the ANN correlation, which was trained with all the data up to 50,000 epochs. The data for low *Re* show some scatter because of the effects of Sr. The predictions agree well with the data in the whole range, and therefore, the effects of *Re* and *Sr* on C_L in Eq. (3.6) can be expressed well with the ANN correlation. Hence, the present ANN structure is expected to be able to correlate the experimental data and additional data simultaneously using Eq. (3.6).

The number of data added to the training set is 17, and the ranges of *Re* and *Sr* are shown in Table 3.4 (the upper three rows in the Table). Only two data points of low *Re* are added in the data of log$M$ =−3.2. On the other hand, 15 data points were added in the low *M* data(logM =−6.6 and −10.6) to supplement the database for a much wider *Re* range. Some data are also added in the intermediate *Re* ranges of $-6.6 \leq \log M \leq -3.2$ to maintain the decreasing trend of the lift curves by the ANN model as shown in **Fig. 3.6**.

Fig. 3.8 shows comparisons between the training data and C_L predicted with the retrained ANN model and lift curves drawn with the model. The predictions agree well with the training data, and the characteristics of the lift curves become more reasonable than the previous predictions (**Fig.3.6**) even with the small number of the additional data. The lift curve for log $M = -10.6$ seems discontinuous at $Re \sim 460$, at which the shape correlation switches between Eqs. (3.3) and (3.4). Even though there are still no training data for $150 < Re < 440$, the trend of the lift curve is accepTable.

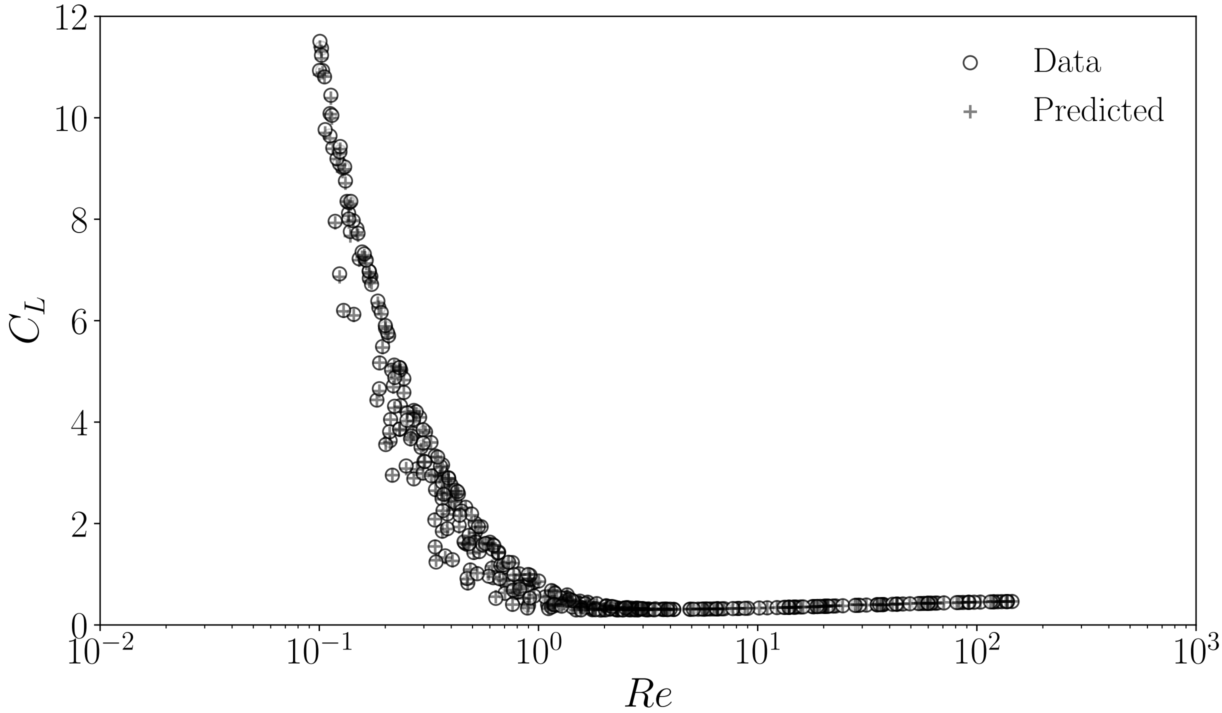

Fig. 3.7 Data created using the Legendre-Magnaudet correlation, Eq. (3.6), (circles) and predictions with ANN correlation (N_l = 3 and N_n = 10) (+ symbols)

Table 3.4: Ranges of Re and Sr in training data added using Eq. (3.5) (upper three rows) and trained ANN model (lower five rows)

M	*Re*	*Sr*	No. of data points
−3.2	0.1 ~ 0.3	0.20 ~ 0.40	2
−6.6	0.1 ~ 4	0.03 ~ 0.06	5
−10.6	0.1 ~ 150	0.02 ~ 0.06	10
-3.2	27 ~ 46	0.12 ~ 0.22	5
-3.9	39 ~ 68	0.10 ~ 0.21	5
−4.8	62 ~ 113	0.084 ~ 0.20	5
−5.5	89 ~ 167	0.074 ~ 0.20	5
−6.6	139 ~ 304	0.054 ~ 0.20	5

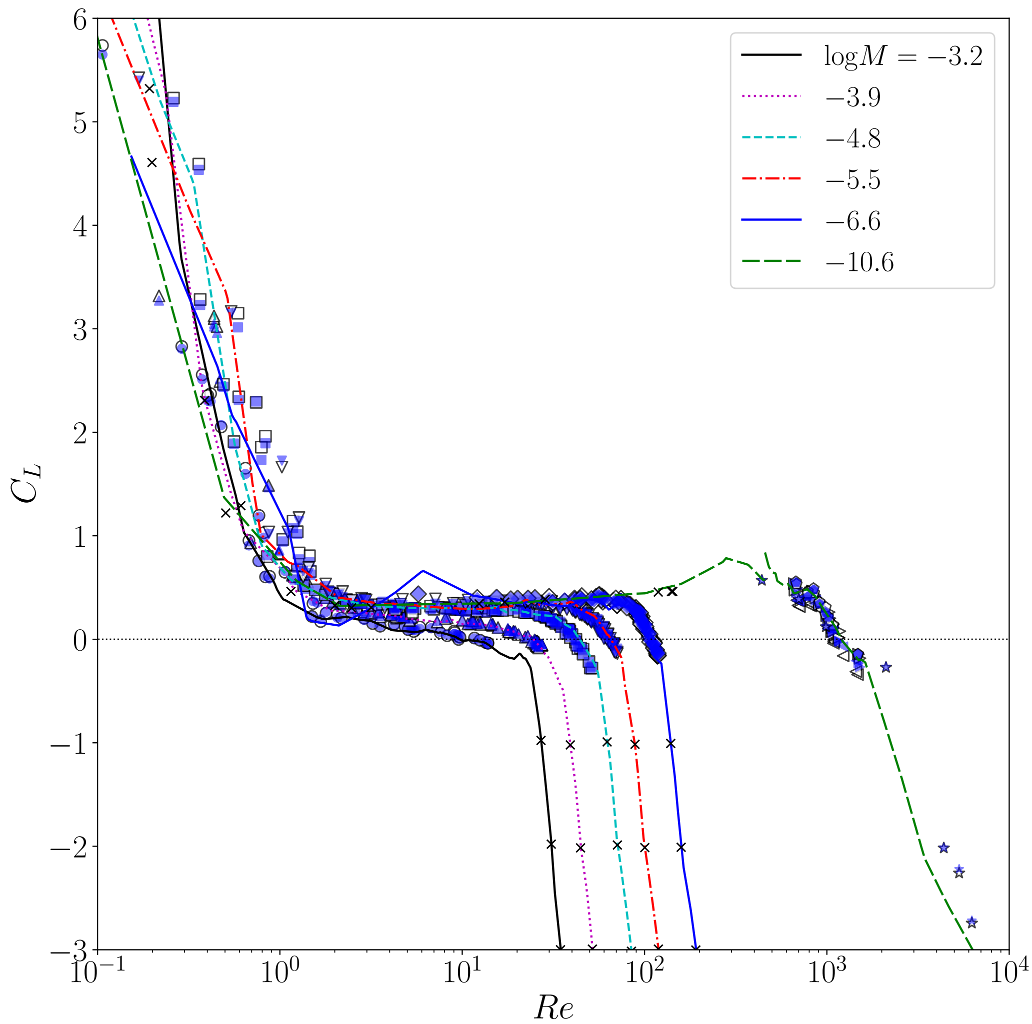

Fig. 3.8 Lift curves drawn using retrained ANN model. Closed symbols: predicted; open symbols: training data; cross symbols: additional data.

3.6 Test phase

The generalization performance of the trained ANN correlation is examined by predicting C_L of the test data. As shown in **Fig. 3.9**, the agreements between the predictions and the test data are fairly well. The characteristics of C_L are reproduced, i.e., C_L decreases with increasing *Re* at low *Re*, the decreasing rate mitigates, and then C_L drops down to the negative lift regime. The errors in the predictions are shown in **Fig. 3.10**. Most data are within ± 10% errors, although some data have relatively larger errors. The developed ANN correlation, thus, does not show remarkable overfitting and has a good generalization performance at least in the parameter ranges tested.

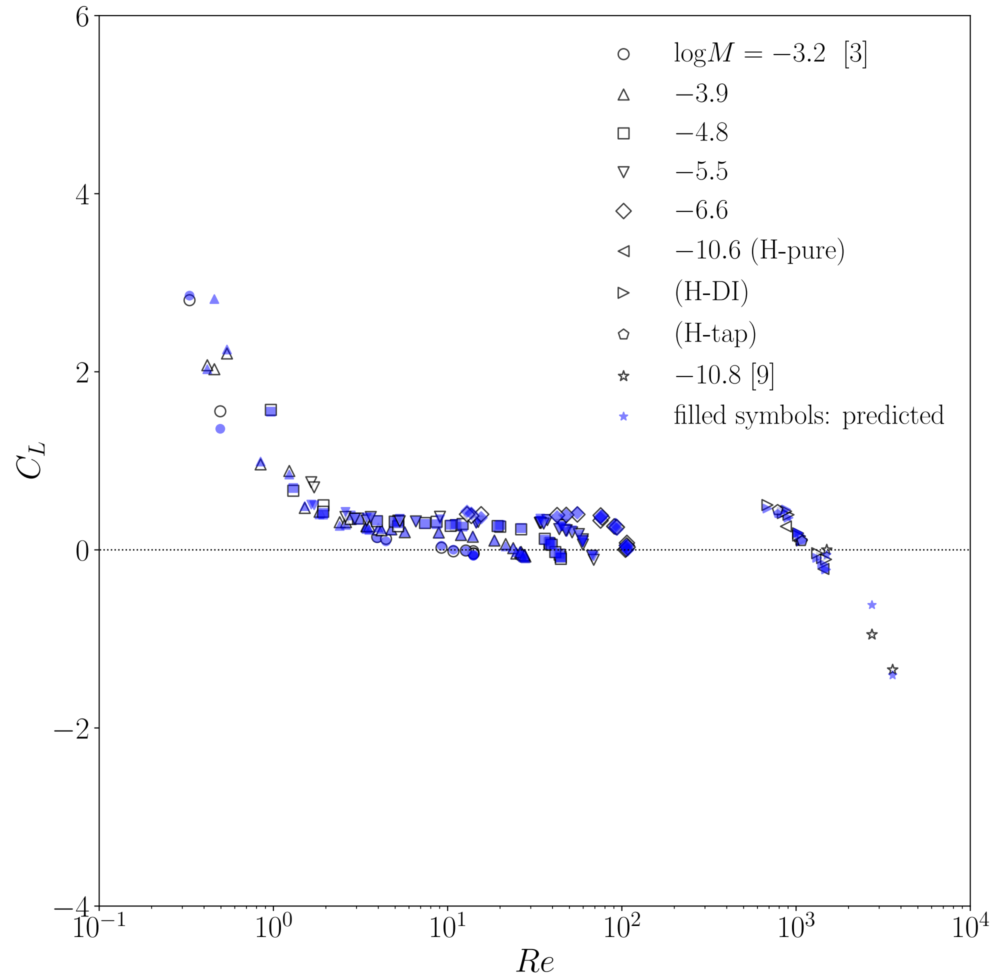

Fig. 3.9 Comparison between predicted C_L with test data (N_l = 3 and Nn = 10). Closed symbols: predicted; open symbols: test data.

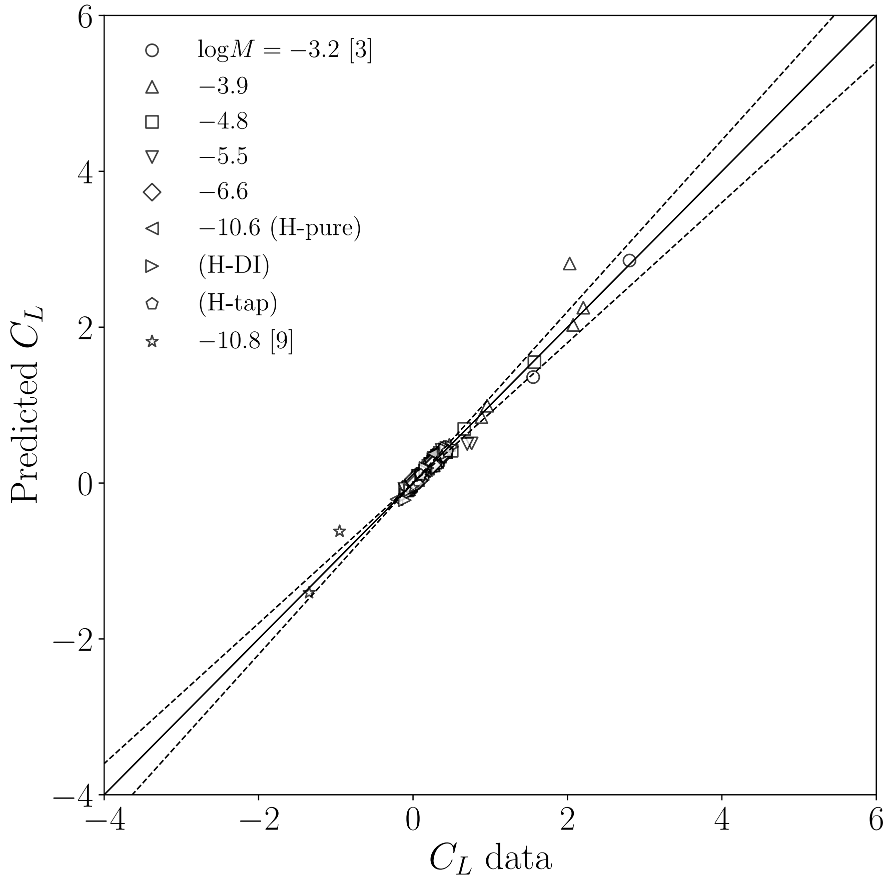

Fig. 3.10 Estimation errors for test data N_l = 3 and Nn = 10. Dashed lines: ± 10% errors.

3.7 Summary

The features of lift coefficients C_L of deformed bubbles in linear shear flows were well expressed by the artificial neural network trained with the experimental databases available in the literature. The K-folds cross validation was used to determine the numbers N_l and N_n of the hidden layers and the neurons, and N_l = 3 and N_n = 10 were selected based on the validation results. The predicted of the C_L agree well with the training data. Comparisons with the test data showed that the developed ANN correlation has a good generalization performance.

The ANN correlation with the simple fully connected network was thus confirmed to be capable of expressing C_L well, and the applicable range covers both viscous force dominant and surface tension-inertial force dominant regimes. The main advantage of the ANN correlation is that the model can be easily improved by adding new lift data.

The simple ANN structure was selected from a point of view of computational costs in bubbly flow simulations. If a C_L data Table is prepared using the ANN and C_L is obtained from the Table in bubbly flow simulations, a more complex structure can be selected for better accuracy. However, overfitting tends to take place for complex structures, and therefore, remedies for overfitting, such as dropout, should be implemented.

References

[1] Nesterov, Y., A Method for Unconstrained Convex Minimization Problem with the Rate of Convergence O(1/k2), Dokl. Akad. Nauk SSSR, vol. 269, no. 3, pp. 543–547, 1983.

[2] He, K., Zhang, X., Ren, S., and Sun, J., Delving Deep into Rectifiers: Surpassing Human-Level Perfor- mance on ImageNet Classification, Proc. of 2015 IEEE Int. Conf. on Computer Vision (ICCV), Santiago, Chile, 2015.

[3] Aoyama, S., Hayashi, K., Hosokawa, S., Lucas, D., Tomiyama, A., 2017. Lift force acting on single bubbles in linear shear flows. International Journal of Multiphase Flow 96, 113–122.

[4] Legendre, D. and Magnaudet, J., The Lift Force on a Spherical Bubble in a Viscous Linear Shear Flow, J. Fluid Mech., vol. 368, pp. 81–126, 1998.

[5] Adoua, R., Legendre, D., and Magnaudet, J., Reversal of the Lift Force on an Oblate Bubble in a Weakly Viscous Linear Shear Flow, J. Fluid Mech., vol. 628, pp. 23–41, 2009.

[6] Tomiyama, A., Tamai, H., Zˇun, I., Hosokawa, S., 2002. Transverse migration of single bubbles in simple shear flows. Chemical Engineering Science 57, 1849–1858.

[7] Hayashi, K., Hessenkemper, H., Lucas, D., Legendre, D., and Tomiyama, A., Scaling of Lift Reversal of Deformed Bubbles in Air-Water Systems, Int. J. Multiphase Flow, vol. 142, p. 103653, 2021.

[8] Hayashi, K., Legendre, D., and Tomiyama, A., Lift Coefficients of Clean Ellipsoidal Bubbles in Linear Shear Flows, Int. J. Multiphase Flow, vol. 129, p. 103350, 2020.

[9] Lee, W. and Lee, J.Y., Experiment and Modeling of Lift Force Acting on Single High Reynolds Number Bubbles Rising in Linear Shear Flow, Exp. Therm. Fluid Sci., vol. 115, p. 110085, 2020.

[10] Aoyama, S., Hayashi, K., Hosokawa, S., Tomiyama, A., 2016. Shapes of ellipsoidal bubbles in infinite stagnant liquids. International Journal of Multiphase Flow 79, 23–30.

[11] Hessenkemper, H., Ziegenhein, T., Lucas, D., and Tomiyama, A., Lift Force Coefficient of Ellipsoidal Single Bubbles in Water, Int. J. Multiphase Flow, vol. 138, p. 103587, 2021.

[12] Ziegenhein, T., Tomiyama, A., and Lucas, D., A New Measuring Concept to Determine the Lift Force for Distorted Bubbles in Low Morton Number System: Results for

Air/Water, Int. J. Multiphase Flow, vol. 108, pp. 11–24, 2018.

[13] Chen, J., Hayashi, K., Hosokawa, S., Tomiyama, A., 2019. Drag correlations of ellipsoidal bubbles in clean and fully-contaminated systems. Multiphase Science and Technology 31(3), 215–234.

[14] Mendelson, H.D., The Prediction of Bubble Terminal Velocities from Wave Theory, Int. J. Multiphase Flow, vol. 13, no. 2, pp. 250–253, 1967.

[15] Legendre, D. and Magnaudet, J., The Lift Force on a Spherical Bubble in a Viscous Linear Shear Flow, J. Fluid Mech., vol. 368, pp. 81–126, 1998.

[16] Legendre, D. and Magnaudet, J., A Note on the Lift Force on a Spherical Bubble or Drop in a Low- Reynolds-Number Shear Flow, Phys. Fluids, vol. 9, pp. 3572–3574, 1997.

[17] Mei, R., Klausner, J., and Lawrence, C., A Note on the History Force on a Spherical Bubble at Finite Reynolds Number, Phys. Fluids, vol. 6, pp. 418–420, 1994.

Chapter 4

Effects of surfactant on lift coefficient of ellipsoidal bubbles in the viscous-force dominant regime

4.1 Introduction

Effects of surfactants on lift coefficients, C_L, of single ellipsoidal bubbles rising through linear shear flows were investigated. Experiment aiming for collecting lift force data was conducted. Two types of surface-active agents, i.e. Triton X-100 and 1-octanol, were used. Making use of a correlation for bubbles in stagnant liquid, a new correlation of drag coefficients was deduced, which agreed well with the experimental data. Different types of surfactant resulted in noticeably different values of C_L especially at low Re. The C_L of small spherical bubbles in contaminated systems could be reproduced by a correlation for solid particles, supporting that fully-contaminated spherical bubbles behave like solid spheres. For deformed bubbles, the lift coefficients can be expressed by relating the negative lift force due to shape deformation with the drag force. Based on the dataset, lift (C_L) correlation for a contaminated bubble was proposed.

4.2. Experimental method

Figure 4.1 shows the experimental setup which consists of an acrylic tank, a stainless seamless belt with a guide, a power system for the belt rotation, a syringe and a nozzle for bubble generation, and an observation system. The width, depth and height of the tank were 200, 110, and 2100 mm, respectively, in which bubbles were rising without wall effect even with their largest size around 4.8 mm. The stainless seamless belt of 100 mm width was tightened by two vertical parallel pulleys and was rotated by a servomotor, generating a steady linear shear flow in the 30 mm gap between the belt and the wall of the acrylic tank. The configuration was the same for clean bubbles [1], however the equipment was updated for the present experiment. The velocity gradient, ω, of the linear shear flow was set at 0.0, 3.2, 4.6, 6.0 and 7.4 s^{-1}. The observation system was composed by two high-speed video cameras (Integrated Design Tools, M5; exposure time: 1/10,000s, framerate: 30-170 flames/s) mounted at z = 150 and 350 mm, respectively, to record bubble displacement for a long-time duration. The spatial resolution was in the range from 0.007 to 0.017 mm/pixel.

The sphere-volume-equivalent bubble diameter d, the bubble velocity $\boldsymbol{V}_B$, and the vertical component of the liquid velocity w_L were measured [1],[2],[3]. Successive bubble images were taken by using two high-speed video cameras, and d and $\boldsymbol{V}_B$ were obtained by using an image processing method [1]. The uncertainties in d and $\boldsymbol{V}_B$ were less than 3% even for the smallest bubble. The spatiotemporal filter velocimetry [4] was employed to obtain w_L in linear shear prior to the experiments of single bubbles. It is confirmed that the measured velocity gradient maintained the same level of accuracy as that in previous study [1]. The C_L was calculated from the measured bubble and liquid velocities, ω and the gas and liquid densities.

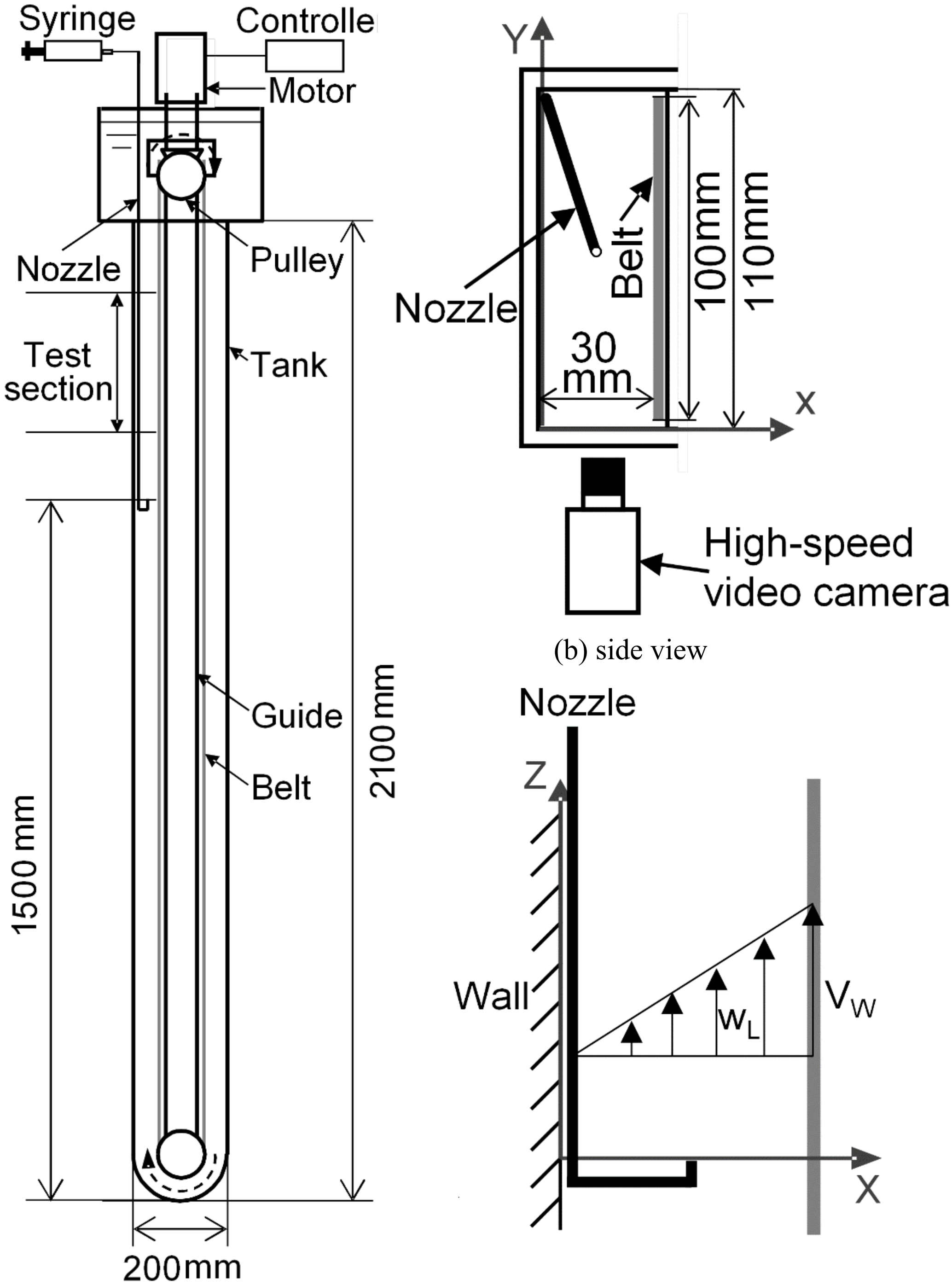

(a) Experimental setup (c) Top view

Fig. 4.1 Experimental setup

The experiments were conducted at room temperature and atmospheric pressure. The liquid temperature was kept at 25±0.5 °C. Contaminated glycerol-water solutions and air were used as the liquid and gas phases, respectively. A clean glycerol-water solution was prepared by mixing water purified by a Millipore system (Merk, Elix 3) and pure glycerol (Kishida-Kagaku). Surfactant was then added to the solution and the solution was re-mixed. Triton X-100 (Wako Pure Chemical Industries, 168-11805) or 1-octanol (Wako Pure Chemical Industries, 156-00136) was used for surfactant. The liquid density and viscosity were measured using a densimeter (Ando keiki Co., Ltd., JIS B7525) and a viscometer (A&D, SV-10), respectively. The surface tension was measured using the pendant bubble method [5]. The uncertainties in the density, viscosity and surface tension estimated at 95% confidence were 0.01, 1.3 and 2.0%, respectively.

The Morton number is defined by

$$M=\frac{\mu_L^4(\rho_L-\rho_G)g}{\rho_L^2\sigma^3} \tag{4.1}$$

where ρ is the density, μ the viscosity, g the acceleration of gravity, σ the surface tension, and the subscripts L and G denote the liquid and gas phases, respectively. **Table 4.1** shows the liquid properties, where σ_0 is the surface tension in clean systems, σ_{eq} the surface tension in adsorption-desorption equilibrium, C_T the concentration of Triton X-100, and C_O the concentration of 1-octanol. The concentration of the glycerol-water solution was 70 wt%, for which $\log M(\sigma_0)$ was −5.5. Given a further increase in surfactant concentration, no change of bubble terminal velocity suggests that the bubble is fully contaminated [6]. Experiments on contaminated bubbles rising through stagnant liquids was also conducted for validation of fully-contaminated systems, the results of which are shown in Sec. 4.4. The Morton number of the system contaminated with Triton X-100 was $\log M(\sigma_{eq}) \sim -5.0$, and the value of C_O was determined to realize the same Morton number $M(\sigma_{eq})$.

Table 4.1 Fluid properties at 25 °C (Glycerol concentration of 70 wt.% (log$M(\sigma_0)$ = −5.5))

	log$M(\sigma_{eq})$	σ_{eq} [N/m]
Clean	−5.5	0.067
C_T = 0.10 mol/m^3	−5.0	0.046
C_T = 0.20 mol/m^3	−4.9	0.042
C_O = 3.25 mol/m^3	−5.0	0.047

*ρ_L = 1178 kg/m^3, ρ_G = 1.2 kg/m^3 and μ_L = 0.018 Pa·s

4.3 Results and discussion

4.3.1 Bubble shape

Examples of bubble shapes in the linear shear flows are shown in **Fig. 4.2**, where E, *Sr* and *Re* are defined by

$$E = \frac{d_V}{d_H} \tag{4.2}$$

$$Sr = \frac{\omega d}{|V_R|} \tag{4.3}$$

$$Re = \frac{\rho_L |V_R| d}{\mu_L} \tag{4.4}$$

where d_V , d_H are the vertical and horizontal reference length of an ellipsoidal bubble respectively, $\boldsymbol{V_R}$ the bubble velocity relative to the liquid velocity. Clean bubbles measured by Aoyama et al. [1] are also shown in the figure. The shape deformation of all contaminated bubbles is smaller than that of clean bubbles. The bubbles in the upper rows at each condition are 2.5-3.0 mm. The presence of surfactant clearly decreases C_L from 0.33 in the clean case to around zero and, in some contaminated cases C_L are negative. It should be noted that *Re* is also reduced by the presence of surfactant while the increase in *Sr* does not substantially affect C_L for these bubbles. The reduction in C_L by surfactant is also clearly observed for the larger bubbles, i.e., the decrease in C_L from the clean case is about 0.2. Negligible effects of *Sr* on C_L are again confirmed.

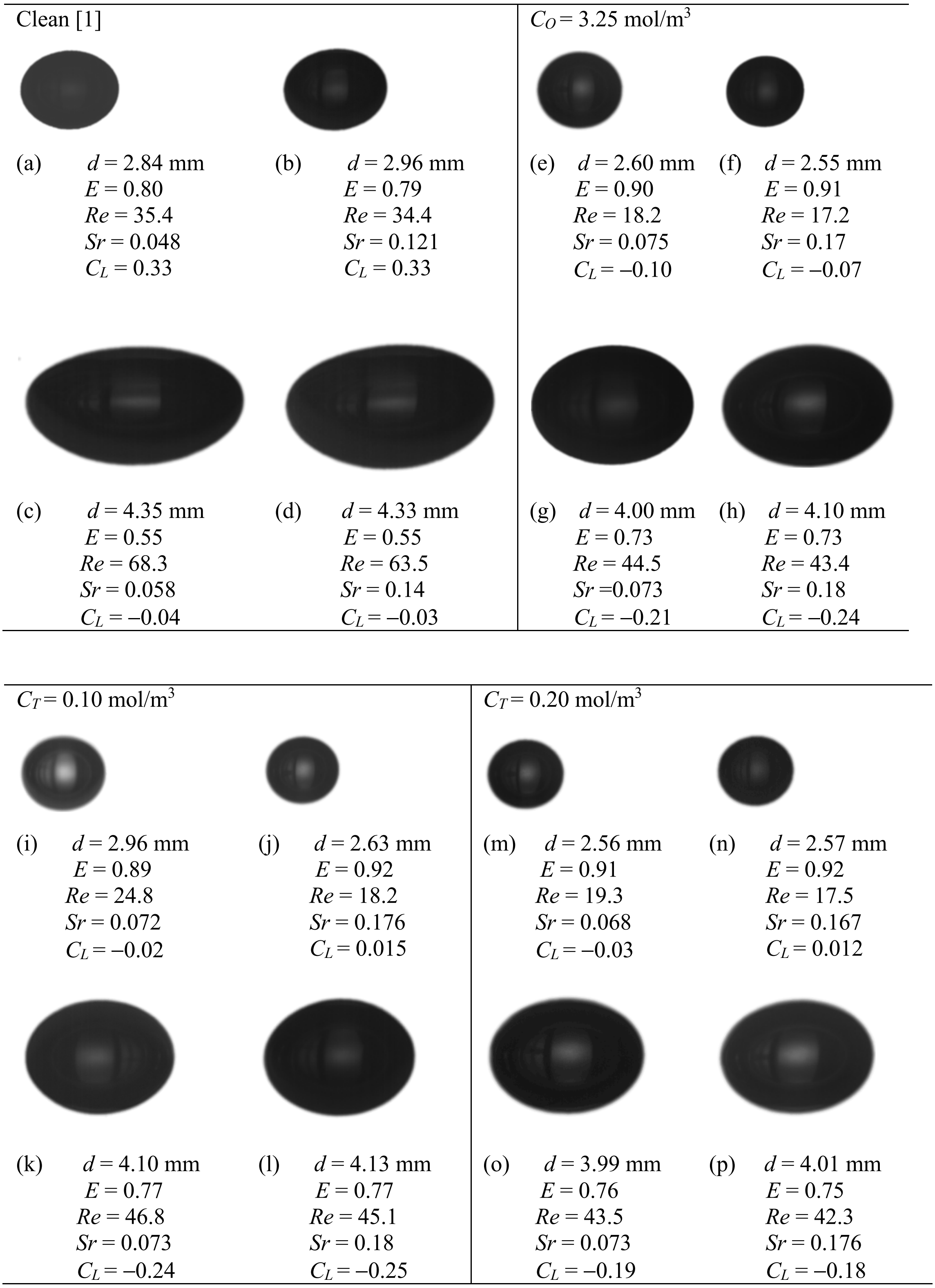

Fig. 4.2 Bubble shapes

4.3.2 Bubble aspect ratio and relative velocity

The aspect ratios are plotted against d in **Fig. 4.3**, in which the data of clean bubbles obtained by Aoyama et al. [1] are also plotted. The E of contaminated bubbles decrease with increasing d and are larger than those of clean bubbles. The deviation from the clean bubble data increases with increasing d. The bubbles in the Triton X-100 cases show slightly weaker deformation than those in the 1-octanol case. In contrast to E, the relative velocities do not depend on the concentration and type of surfactant as shown in **Fig. 4.4**, i.e., the systems are fully-contaminated from the point of view of bubble velocity. The difference in E may therefore ascribe to unique absorption-desorption characteristics corresponding to a type of surfactants [7]. Dependence of E on Sr is not remarkable as in clean bubbles [1] implying that a correlation of E for bubbles in stagnant liquids is applicable to bubbles in the linear shear flows.

Aoyama et al. [1] proposed the following correlation of E for contaminated bubbles in stagnant liquid adopting σ_{eq} as one of its indispensable factors responsible for the shape deformation:

$$E=\frac{1}{[1+0.024Eo(\sigma_{eq})^{1.17}Re^{0.44}]^{0.57}} \tag{4.5}$$

Table 4.2 shows the mean absolute error (MAE) and root mean squared error (RMSE) of the calculated aspect ratios using Eq. (4.5). The correlation gives good results.

Table 4.2 Mean absolute error and root mean squared error in calculated aspect ratios

	MAE	RMSE
C_T = 0.10 mol/m^3	0.00471	0.00691
C_T = 0.20 mol/m^3	0.00751	0.01050
C_O = 3.25 mol/m^3	0.01340	0.01740
Average	0.00854	0.01160

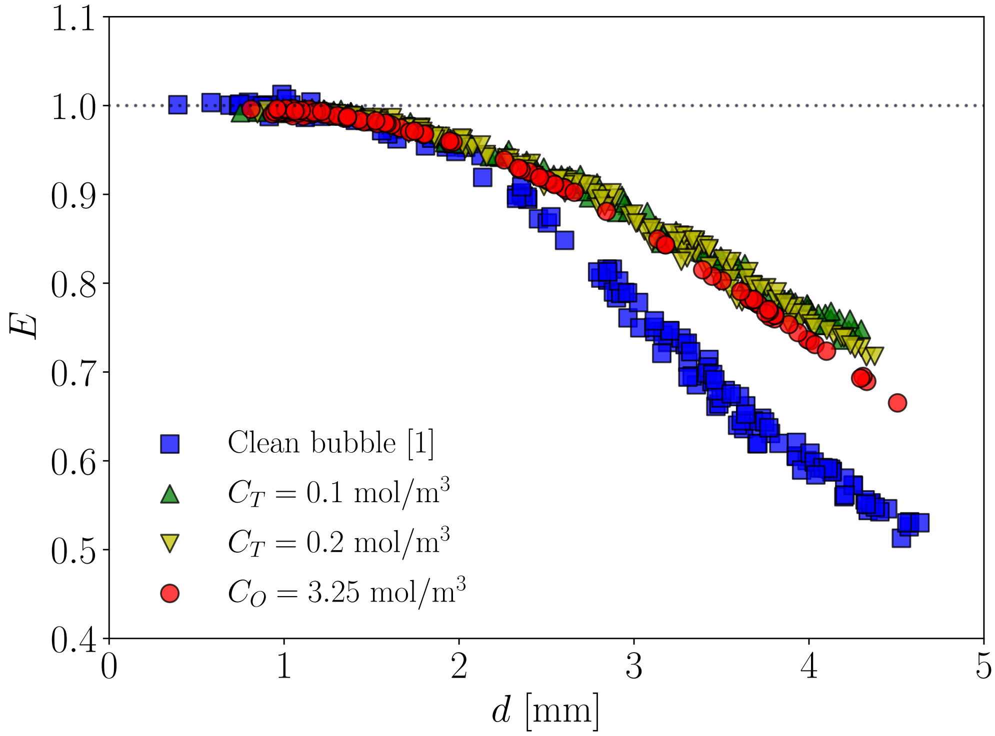

Fig. 4.3 Bubble aspect ratio

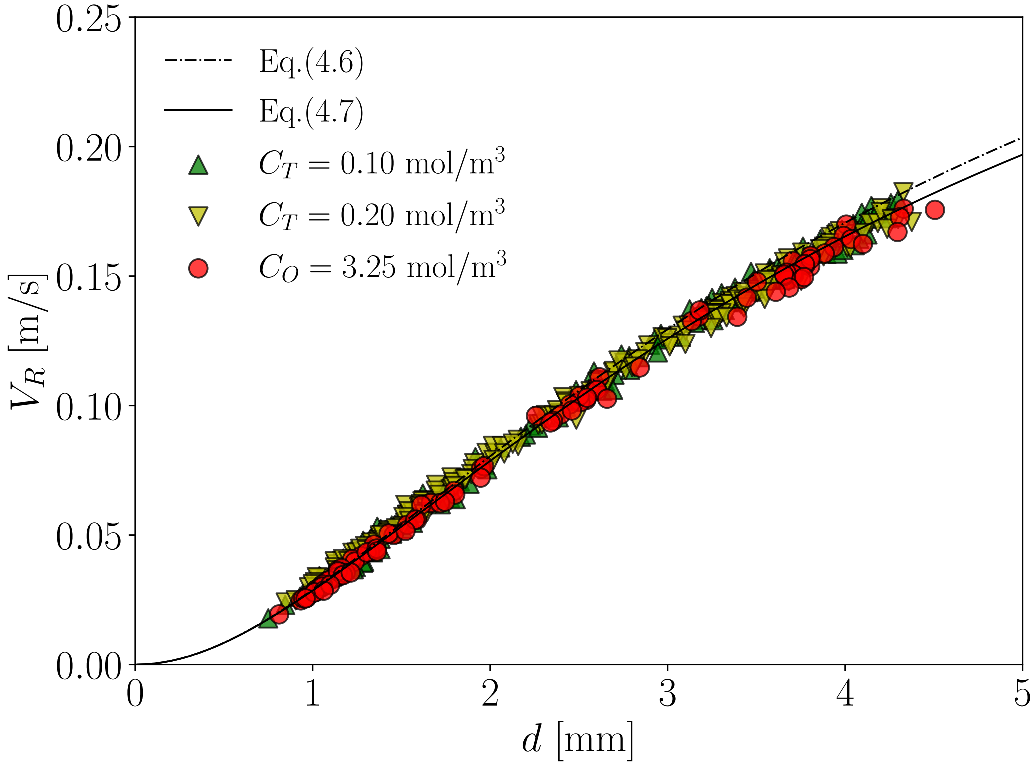

Fig. 4.4 Bubble relative velocity

The dotted line in **Fig. 4.4** represents $|\boldsymbol{V}_R|$ calculated with the following drag correlation for fully-contaminated bubbles in infinite stagnant liquids [8]:

$$C_D = \frac{24}{Re}\left(1 + \frac{0.15Re^{0.687}}{E^{0.48}}\right) \tag{4.6}$$

where E was calculated using Eq. (4.5). Although the correlation gives reasonable values, the data are somewhat smaller than the curve at large d. Legendre and Magnaudet [9] reported that C_D of spherical bubbles in shear flows increases with Sr at high Re and developed a C_D correlation that is represented by a combination of C_D in a uniform flow and a multiplier $[1 + \alpha Sr^{\beta}]$, where α and β are constants. Aoyama et al. [1] also recognized a slight Sr effect for clean ellipsoidal bubbles at small and intermediate Re. Below is the following C_D correlation for contaminated bubbles with the Sr effect by adopting the multiplier with the coefficients tuned for the present data:

$$C_D = \frac{24}{Re}\left[1 + \frac{0.15Re^{0.687}}{E^{0.48}}(1 + 222Sr^{4.25})\right] \tag{4.7}$$

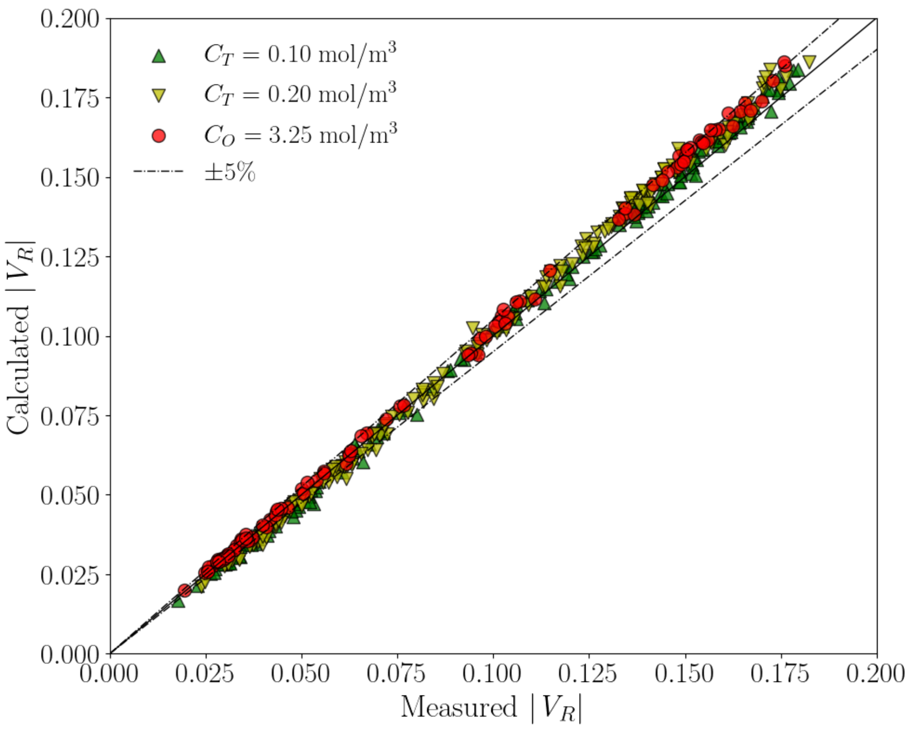

Fig. 4.5 Comparison between predicted and measured $|\boldsymbol{V}_{\mathrm{R}}|$

Figure 4.5 shows the comparison between the $|V_R|$ predicted by using Eq. (4.7) and data. By accounting for the *Sr* effect Eq. (4.7) well predicts the velocity data, and MAE for Eq. (4.7) is 5.65 x 10^{-6} m/s, which is smaller than 1.90 x 10^{-5} m/s for Eq. (4.6).

4.3.3 Lift coefficient

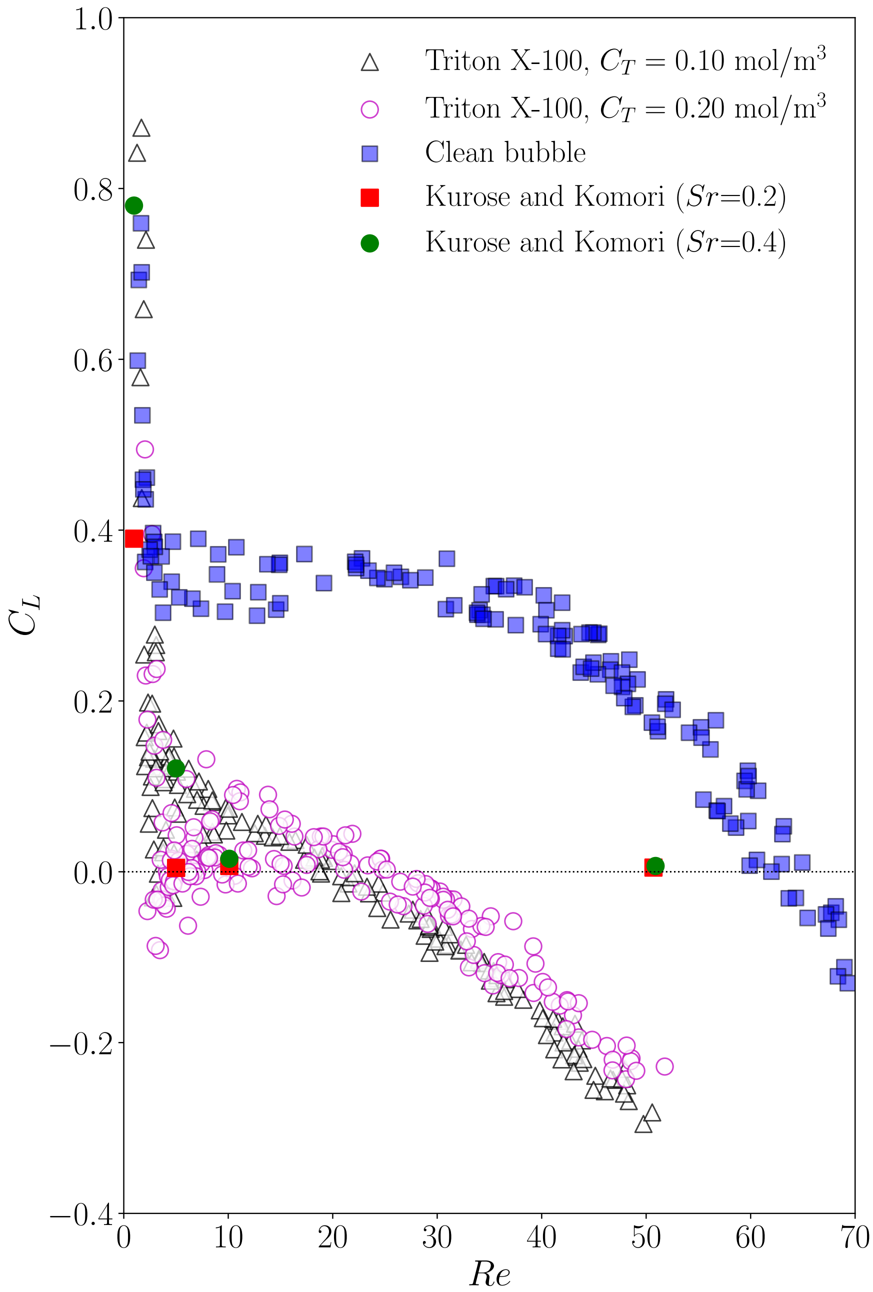

Fig. 4.6 Lift coefficients in clean and cases of C_T = 0.10 and 0.20 mol/m^3

Figure 4.6 shows C_L of $C_T = 0.10$ mol/m^3 and 0.20 mol/m^3. The clean bubble data [1] are also plotted for comparison. Both clean and contaminated data show a similar tendency, i.e., after a steep decrease to a local minimum, further increase in *Re* causes slight increase in C_L and then decrease to the negative values. The C_L of contaminated bubbles are however much lower than those of clean bubbles and the reversal of C_L due to bubble deformation occurs at smaller *Re*. The surfactant concentration shows only a small influence on C_L.

It is well known that C_D of fully-contaminated spherical bubbles agree well with those of solid spheres due to the Marangoni stress. Kurose and Komori [10] conducted numerical simulations of solid spheres in linear shear flows. Their numerical data at *Sr* = 0.2 and 0.4 are plotted in **Fig. 4.6**. The C_L of solid spheres depends on *Sr* for $Re \sim 5$ and becomes almost zero for $Re \geq 10$. The C_L of contaminated bubbles are close to those of solid spheres for $Re < 10$, though it is difficult to recognize clear dependence on *Sr* in the bubble case. As *Re* increases, C_L of contaminated bubbles deviate from those of solid spheres due to bubble deformation, which is similar to the relationship between clean spherical bubbles and ellipsoidal bubbles as mentioned in the introduction [9],[1],[11],[12].

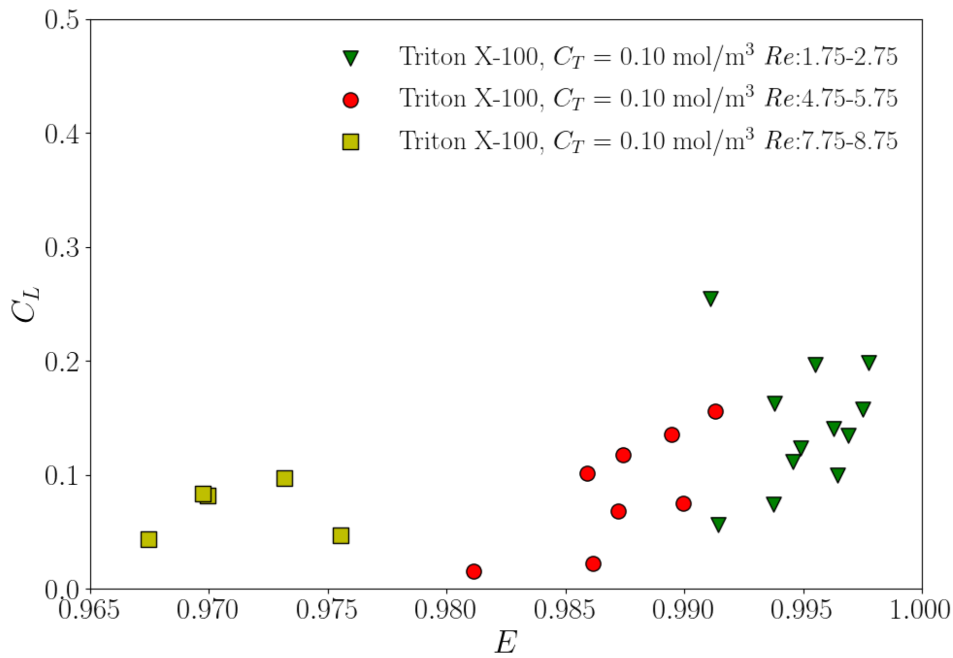

Fig. 4.7 C_L in Triton X-100 case at low *Re* range

The Triton X-100 data shows some scattering in the range of *Re* from 2 to 20 and converges afterward. A possible explanation to this is that bubbles adopt different shapes even at the same *Re* due to different degree of surfactant accumulation at the interface. **Fig. 4.7** shows Triton X-100 data selected according to different *Re* ranges as indicated by the legends. It can be readily noticed that bubble shapes show a relatively large variation even within the narrow *Re* range, which explains the reason of the scatter of C_L. The different surfactant distributions at bubble interface can be ascribed to a long time constant of surfactant adsorption/desorption, which may add uncertainties in reaching the steady state as pointed out by Zhang and Finch [13]. It is interesting that the scatter is pronounced only in the narrow *Re* range (5 ～20) and mitigates at larger *Re* where the negative lift is dominant in C_L.

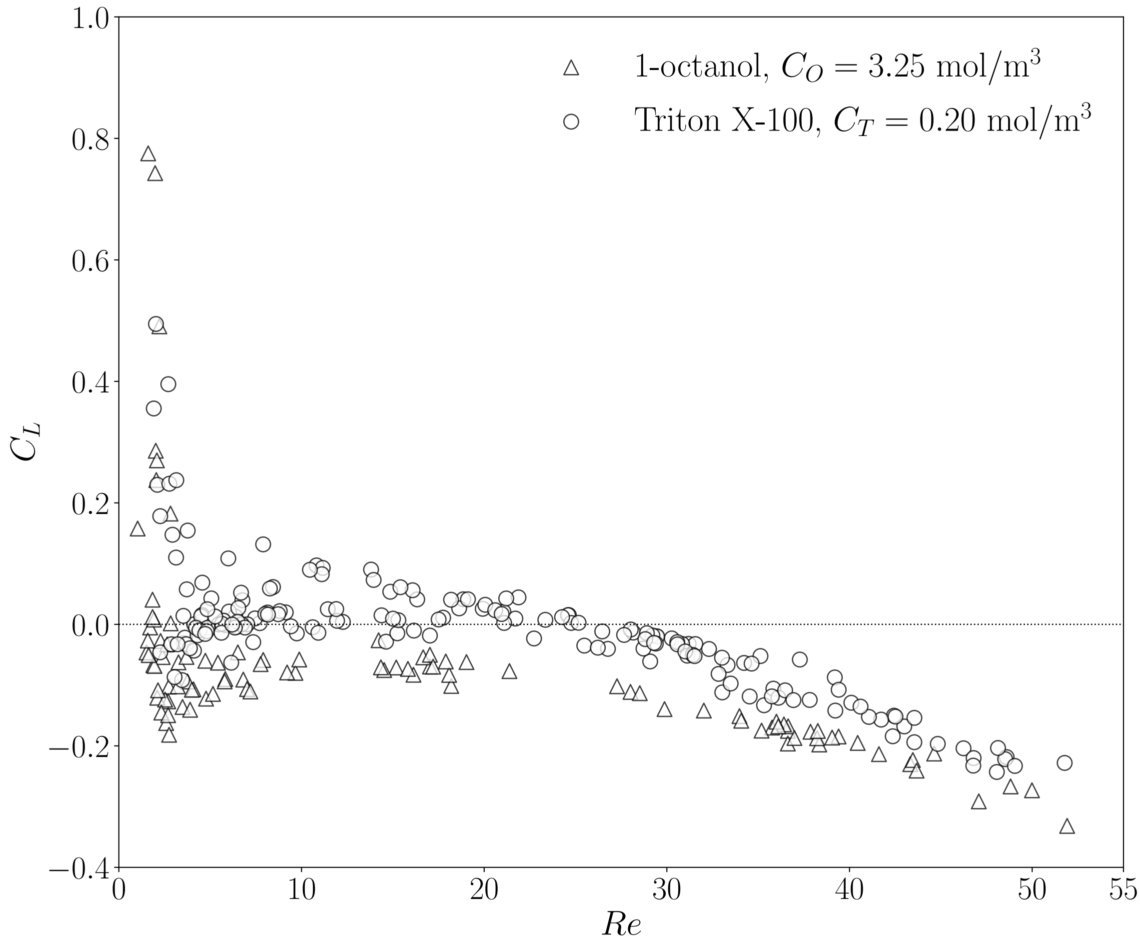

Fig. 4.8 Comparison between C_L of bubbles contaminated with Triton X-100 and those with 1-octanol

Figure 4.8 shows C_L for two kinds of surfactants. The difference in σ_{eq} is negligibly small as shown in **Table 4.1**, enabling to focus on the difference in the type of surfactants. The C_L with 1-octanol decreases to the local minimum at smaller *Re* than that with Triton X-100 and the two sets of data slightly increase and then decrease with increasing *Re*. The tendency that the deviation of these two sets of data become reduced as the increase of *Re* suggests that small bubbles are particularly subject to the ad-desorption kinetics of surfactant, in other words the surfactant distribution at the interface, whereas shape deformation plays a dominant role in C_L as bubbles become larger. In addition, the difference between these sets of results can only be ascribed to an effect of different types of surfactants and deserves further research. The small scatter for $5 < Re < 20$ in the 1-octanol case can be described by the larger Langmuir number than in the Triton X-100 case [7].

4.3.4 Lift correlating

Hayashi et al. [11] pointed out that the drag and the negative lift of clean bubbles of Re >> 1 are related as

$$C_L = C_L^{S\infty} - G(E, Re)C_D \tag{4.8}$$

where $C_L^{S\infty}$ = 1/2 [14], and $G(E, Re)$ is a function of E and Re. For the lift reversal in the viscous force dominant regime, they obtained the following expression of C_L, which explicitly includes the vorticity produced at the bubble interface:

$$C_L = C_L^{S\infty} - \gamma \frac{16}{Re} \phi(E, Re) \omega_{\max}^{*\infty}(E) \tag{4.9}$$

where γ = 0.078, $\omega_{\max}^{*\infty}$ is the dimensionless maximum vorticity in the infinite Reynolds number limit given by Magnaudet and Mougin [15]

$$\omega_{\max}^{*\infty}(\mathrm{E}) = \frac{2E^{-8/3}(1-E^2)^{3/2}}{\sin^{-1}\sqrt{1-E^2} - E\sqrt{1-E^2}} \tag{4.10}$$

and ϕ (E, Re) is the deformation-inertia factor in the drag correlation proposed in Sec. 2 [8]:

$$C_D = \frac{16}{Re}[1+\phi(E, Re)] \tag{4.11}$$

where

$$\phi(E, Re) = 0.25E^{-1.9}Re^{0.32} \tag{4.12}$$

By assuming that the negative lift of fully-contaminated bubbles has a relation similar to Eq. (4.8) and employing Eq. (4.7) for the drag, Eq. (4.9) can be written as:

$$C_L = C_L^B - \gamma' \frac{16}{Re} \phi_c(E, Re) \alpha' E^{\beta'} \tag{4.13}$$

where $\phi_c(E,Re)=0.15E^{-0.48}Re^{0.68}(1+222Sr^{4.25})$ and $\alpha' E^{\beta'}$ epitomizes $\omega_{max}^{*\infty}$, whose analytical expression for rigid ellipsoids has not been obtained. The constant 16 is adopted for the factor of Re^{-1} rather than 24 since the multiplier 3/2 due to the difference in the boundary condition at the interface should be involved in $\omega_{max}^{*\infty}$ [9]. The C_L of a clean spherical bubble approaches 0.5 as $Re \rightarrow \infty$ and that of spherical solid particle becomes very close to zero in that limit [10]. In the Triton X-100 data, C_L seems to follow $C_L = 0.1$ if no deformation was assumed even at intermediate Re. On the other hand, the 1-octanol data show that C_L steeply decreases and enters to the negative lift regime at small Re. Therefore, the baseline, C_L^B, for the spherical part may be different for those cases.

The coefficients γ', α', β' and C_L^B, were fitted to the data as shown in **Table 4.3**. As shown in **Fig. 4.9**, the C_L data in the negative lift regime can be well reproduced. For the clean bubbles, $\omega_{max}^{*\infty} \propto E^{-8/3}$ where E becomes small [16]. $\beta' = -6$ is much smaller than this limiting value for clean bubbles, implying that the contaminated interfaces with no-slip boundary condition produce larger vorticity with increasing shape deformation compared with the slip condition. The β' takes the same value in both cases, which is consistent with the fact that bubbles in both cases are fully-contaminated.

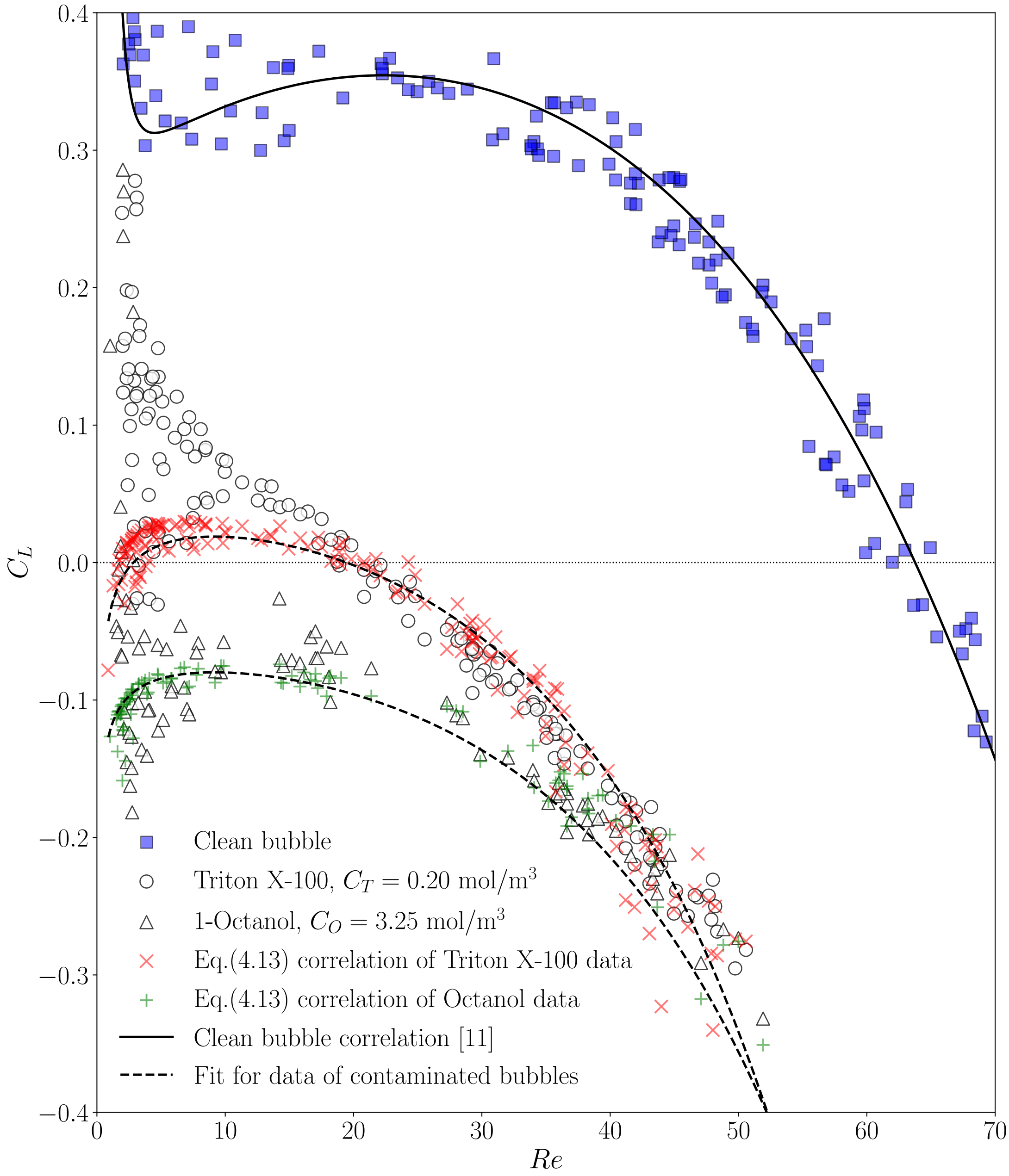

Fig. 4.9 Correlation of negative lift

Table 4.3 Coefficients in Eq. (4.13)

	$C_T = 0.20$ mol/m^3	$Co = 3.25$ mol/m^3
C_L^B	0.11	- 0.01
$\gamma'\alpha'$	0.06	0.046
β'	- 6	- 6

4.4 The Application of deep learning method of contaminated data

Chapter 3 has demonstrated that the ANN method is applicable to clean data and gives good results. The major features (Re, Eo, Sr, E, C_L) of the contaminated data are the same as thoes of the clean data. Therefore, it is worth applying the ANN method given in chapter 3 to the contaminated data. The experiment data are divided into two sets. The size of the test set is 91 while the size of the training set is 361. The neural network is fully connected and contains 3 hidden layers and 10 neurons by which the optimized accuracy can be reached. The steep descent gradient method is used to update the parameters. To show the performance of the ANN method, **Figs. 4.10** and **4.11** are plotted using the test data and the predicted data. As shown in **Fig. 4.10**, the agreements between the predictions and the test data are acceptable, showing the capability of this method. The errors in the predictions are shown in **Fig. 4.11**. Most data are within ± 10% errors. The developed ANN correlation does not show remarkable overfitting and has a good performance for the contaminated data.

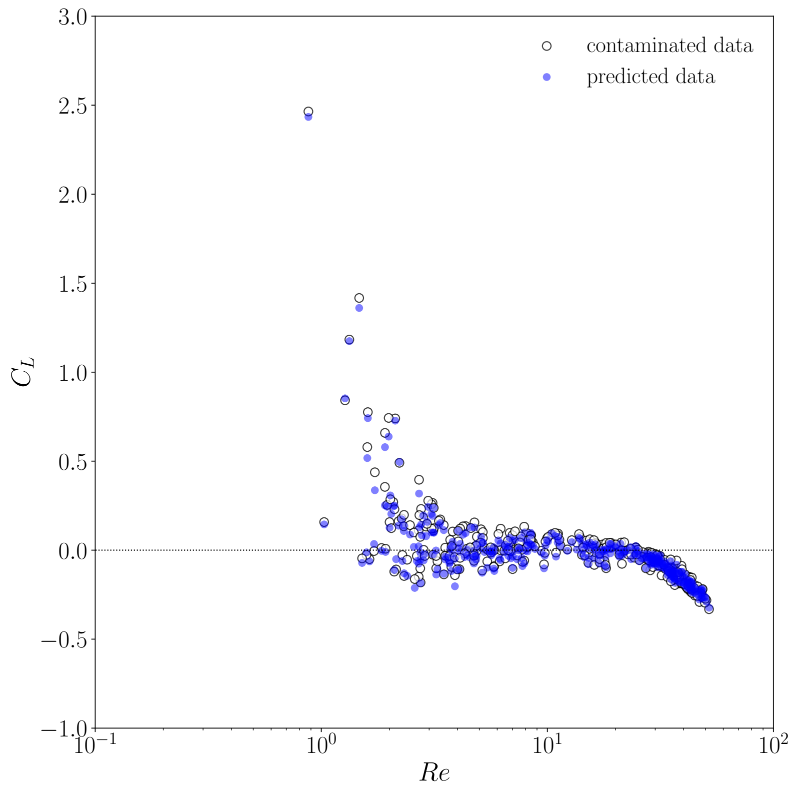

Fig. 4.10 Comparison between predicted C_L with test data (N_l = 3 and Nn = 10).

Closed symbols: predicted; open symbols: test data.

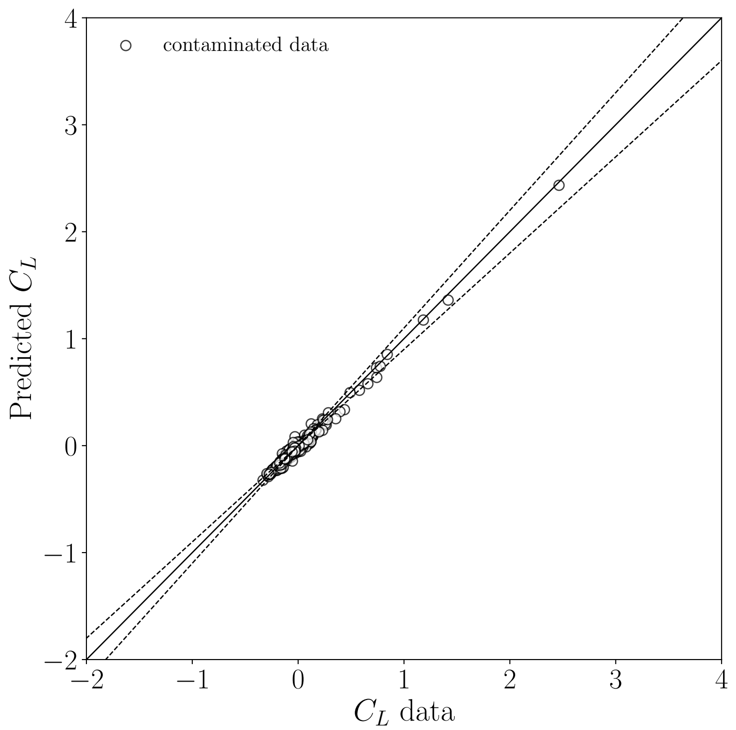

Fig. 4.11 Estimation errors for test data N_l = 3 and Nn = 10. Dashed lines: ± 10% errors.

4.5 Summary

Single bubbles rising in a linear shear flow of a glycerol-water solution contaminated with two types of surfactants were measured to obtain C_L data. Triton X-100 and 1-octanol were used as surfactants. Two high-speed cameras recorded bubble lateral migration, from which bubble shapes, relative velocities and lift coefficients were obtained. The bubble Reynolds number *Re* ranged from 0.87 to 70. The dimensionless shear rate ranged from 0 to 0.25. The effect of types and concentration of surfactants on the lift coefficient were also discussed. As a result, the following conclusions were obtained:

(1) The dimensionless shear rate is not a dominant factor causing the change in shape deformation, so that an available shape correlation for bubbles in stagnant liquid can be used to estimate the bubble aspect ratio.

(2) Both clean and contaminated C_L data have similar tendency that after a drastic decrease to a local minimum, C_L value slightly increases and then gradually falls to negative lift regime.

(3) A difference in the concentration of identical surfactant results in a slight change of C_L of fully-contaminated bubbles persisting to high Re regime.

(4) Different types of surfactants result in different values of C_L even under the fully-contaminated condition.

(5) A negative lift component related with the drag force describes well the lift reversal for contaminated bubbles as well as for clean bubbles.

(6) The ANN method gives a good performance for the contaminated data.

References

[1] Aoyama, S., Hayashi, K., Hosokawa, S., and Tomiyama, A., 2017. Lift force acting on single bubbles in linear shear flows. Int. J. Multiphas. Flow, 96. 113-122.

[2] Ogawa, K., Myint, W., Hosokawa, S., and Tomiyama, A., 2007. Study on lift force acting on single drops in linear shear flows. Prog. Multiphase Flow Res., 2, 55-62 (in Japanese).

[3] Tomiyama, A., 2004. Drag, lift and virtual mass forces acting on a single bubble. Proc. 3rd Int. Symposium on Two-phase Flow Modelling and Experimentation. Pisa.

[4] Tomiyama, A., Celata, G. P., Hosokawa, S., and Yoshida, S., 2002a. Terminal velocity of single bubbles in surface tension force dominant regime. Int. J. Multiphas. Flow, 28, 1497-1519.

[5] Lin, S. Y., McKeigue, K., and Maldarelli, G., 1990. Diffusion-controlled surfactant adsorption studied by pendant drop digitization. AIChE J., 36, 1785-1795.

[6] Aoyama, S., Hayashi, K., Hosokawa, S., and Tomiyama, A., 2018. Shapes of single bubbles in infinite stagnant liquids contaminated with surfactant. Exp. Therm. Fluid Sci., 96. 460-469.

[7] Hayashi, K., and Tomiyama, A., 2018. Effects of surfactant on lift coefficients of bubbles in linear shear flows. Int. J. Multiphas. Flow, 99, 86-93.

[8] Chen, J., Hayashi, K., Hosokawa, S., Tomiyama, A., 2019. Drag correlations of ellipsoidal bubbles in clean and fully-contaminated systems. Multiphase Science and Technology 31(3), 215–234.

[9] Legendre, D., and Magnaudet, J., 1998. The lift force on a spherical bubble in a viscous linear shear flow. J. Fluid Mech., 368, 81-126.

[10] Kurose, R., and Komori, S., 1999. Drag and lift forces on a rotating sphere in a linear shear flow, 384, 183-206.

[11] Hayashi, K., Legendre, D., and Tomiyama, A., 2020. Lift coefficients of clean ellipsoidal bubbles in linear shear flows. Int. J. Multiphas. Flow, 129, 103350.

[12] Hayashi, K., Hessenkemper, H., Lucas, D., Legendre, D., Tomiyama, A., 2021, Scaling of Lift Reversal of Deformed Bubbles in Air-Water Systems, Int. J. Multiphas. Flow, 142, 103653.

[13] Zhang, Y., & Finch, J., 2001. A note on single bubble motion in surfactant solutions. J. Fluid Mech., 429, 63-66.

[14] Auton, T. R., 1987. The lift force on a spherical body in a rotational flow. J. Fluid Mech., 183, 199-218.

[15] Magnaudet, Jacques & Mougin, Guillaume. 2007. Wake instability of a fixed spheroidal bubble. Journal of Fluid Mechanics. 572. 10.1017/S0022112006003442.

[16] Adoua, R., Legendre, D., and Magnaudet, D., 2009. Reversal of the lift force on an oblate bubble in a weakly viscous linear shear flow. J. Fluid Mech., 628, 23-41.

Chapter 5

Conclusions

Two-phase flow is a ubiquitous phenomenon in both industry and nature such as bubbly flows in a bubble column, and a cooling system in a nuclear plant. In industrial applications the enhancement of safety and efficiency cannot be achieved without sufficient knowledge on the motion of bubbles. Being subjected to shear and pressure forces, single bubbles may show lateral migration while rising, resulting in non-uniform void distribution. Drag force determines the terminal velocity of single bubbles. Lift force, which is primarily induced by shear flow, plays a crucial role in lateral displacement of a bubble. Available drag correlations for bubbles in the viscous force dominant regime take relatively complicated functional forms and their applicable range is narrow. Lift correlations have been suggested analytically without the support of experimental data and empirical correlations covering a wide range of fluid properties are still unavailable, especially for a bubble in contaminated system.

In this dissertation, new drag force correlations (C_D) adopting relatively simple form was deduced which is applicable to a wide range of Reynolds number in both clean and contaminated systems. Experiment aiming at collecting lift data of single bubble rising in linear shear flow was conducted with the presence of several kinds of surfactant. Effects of surfactant were discussed and lift (C_L) correlation for a contaminated bubble was proposed. Deep learning method was applied to C_L data in clean system. Predicted data generated by optimized training models agrees well with test data.

In chapter 2, effects of surfactant and bubble aspect ratios on the terminal velocity of single ellipsoidal bubbles rectilinearly rising through stagnant liquids were investigated to develop a reliable drag coefficient, C_D for fully-contaminated bubbles in the viscous-force dominant regime. Triton X-100, 1-octanol, 1-decanol and SDS were used for surfactant in the experiments. It was clarified that C_D of fully contaminated bubbles does not depend on the type of surfactants. Therefore, C_D correlation was developed using the bubble Reynolds number (Re) and the aspect ratio (E). The proposed C_D correlation for contaminated systems is simpler than available correlations but agrees well with a wide range of experiment data, i.e. $-8.0 \leq \log M \leq -3.2$, $0.53 \leq Re \leq 166$ and $0.12 \leq Eo \leq 8.2$, where M is the Morton number and Eo the Eötvös number. Following the same form as in the contaminated system, C_D correlation in a clean system was also formulated ,which gives good predictions of V_T for $-11 \leq \log M \leq 0.63$, $3.2\times10^{-3} \leq Re \leq 720$ and $0.042 \leq Eo \leq 29$.

In chapter 3, an artificial neural network (ANN) correlation for the lift coefficient C_L of spherical and deformed bubbles in linear shear flows was developed. Three hidden layers were confirmed to give optimal fitting efficiency. Input features selected were the bubble Reynolds number, the Eötvös number, the dimensionless shear rate, and the bubble aspect ratio. The output was C_L only. The training and test data included bubbles in viscous force dominant and surface tension-inertial force dominant regimes. Good agreements between the training data and model predictions confirmed the applicability of the ANN correlation to the lift coefficient. It was also shown that the model is easily improved by new data transfusion. The simple ANN structure was selected from a point of view of computational costs in bubbly flow simulations. In other words, if a C_L data table is prepared using the ANN and C_L is obtained from the table in bubbly flow simulations, a more complex structure can be selected for better accuracy.

In chapter 4, effects of surfactants on lift coefficients, C_L, of single ellipsoidal bubbles rising through linear shear flows were investigated. Two kinds of surfactant, Triton X-100 and 1-octanol were used. The range of the bubble Reynolds number was $0.1 < Re < 70$ and $\log M = -5.5$. Bubble shapes were either spherical or ellipsoidal. Compared with clean bubbles, less deformation of contaminated bubbles was confirmed since surfactant tends to accumulate on the bubble interface, rendering it to behave like solid particles. A shape correlation without taking the dimensionless shear rate into account gave good evaluations of the bubble aspect ratio, which means that the shear rate is not a dominant factor causing the shape deformation. However drag coefficients were affected by the shear rate. Using the correlation developed for bubbles in stagnant liquid, a new drag correlation accounting for the shear effect was deduced, which agreed well with the experimental data. Both clean and contaminated C_L data showed similar tendency, i.e., after a drastic decrease to a local minimum, C_L value slightly increases with increasing the bubble Reynolds number, and then gradually decreases to negative values. A difference in concentration of Trion X-100 resulted in only a slight change in C_L at high *Re*. Different types of surfactants resulted in noticeably different values of C_L especially at low *Re*. The C_L of small spherical bubbles in contaminated systems agreed with the C_L data for solid particles, supporting that fully-contaminated spherical bubbles behave like solid spheres. For deformed bubbles, the lift coefficients were well correlated by relating the negative lift force due to shape deformation with the drag force. The ANN method is also applied for contaminated data and received good results.

Above are the conclusions derived from this study. Both C_D and C_L are proved to be accurate correlations for the prediction of drag and lift forces of single bubbles rising in linear shear flow. ANN method can generate reliable C_L data from optimized training model and is easily alterable for performance enhancement by feeding new data to ANN correlation.

Doctoral Dissertation, Kobe University

“Study on drag and lift force acting on single bubbles rising in linear shear flows ”, 82 pages

Submitted on January, 20, 2023
The data of publication is printed in cover of repository version published in Kobe University